Chapter 1
Self-accelerating Airy Beams: Generation, Control, and Applications

Yi Hu, Georgios A. Siviloglou, Peng Zhang, Nikolaos K. Efremidis, Demetrios N. Christodoulides, and Zhigang Chen

1.1 Introduction

More than three decades ago, Berry and Balazs made an important prediction within the context of quantum mechanics: they proposed theoretically that the Schrödinger equation describing a free particle can exhibit a nonspreading Airy wave packet solution [1]. Perhaps, the most remarkable feature of this Airy packet is its ability to *freely accelerate* even in the absence of any external potential. As first noted in Berry's paper, this Airy packet happens to be unique, e.g., it is the only nontrivial solution (apart from a plane wave) that remains invariant with time

Y. Hu (✉)
Department of Physics and Astronomy, San Francisco State University, San Francisco, CA 94132, USA

The Key Laboratory of Weak-Light Nonlinear Photonics, Ministry of Education and TEDA Applied Physics School, Nankai University, Tianjin 300457, China

INRS-EMT, University of Quebec, 1650 Blvd. Lionel Boulet, Varennes, QC, Canada J3X 1S2, e-mail: hynankai@gmail.com

G.A. Siviloglou • D.N. Christodoulides
CREOL/College of Optics, University of Central Florida, Orlando, FL 32816, USA

P. Zhang
Department of Physics and Astronomy, San Francisco State University, San Francisco, CA 94132, USA

N.K. Efremidis
Department of Applied Mathematics, University of Crete, Heraklion, Crete 71409, Greece

Z. Chen
Department of Physics and Astronomy, San Francisco State University, San Francisco, CA 94132, USA

The Key Laboratory of Weak-Light Nonlinear Photonics, Ministry of Education and TEDA Applied Physics School, Nankai University, Tianjin 300457, China

Z. Chen and R. Morandotti (eds.), *Nonlinear Photonics and Novel Optical Phenomena*, Springer Series in Optical Sciences 170, DOI 10.1007/978-1-4614-3538-9_1,

in one-dimensional (1D) domain [1, 2]. However, this work has hibernated in the literature for decades, and it never led to experimental realization of any self-accelerating Airy wave packet.

Over the years, nonspreading or nondiffracting wave configurations have been systematically investigated in higher-dimensions (2D and 3D), particularly in the areas of optics and atom physics [3–8]. What makes the analogy between these two seemingly different disciplines possible is the mathematical correspondence between the quantum mechanical Schrödinger equation and the paraxial equation of diffraction [9]. In terms of experimental realization, optics has thus far provided a fertile ground in which the properties of such nonspreading localized waves can be directly observed and studied in detail. Perhaps, the best known example of such 2D diffraction-free optical waves is the so-called *Bessel beams* as first suggested and observed by Durnin et al. [3, 4]. This work has since sparked considerable theoretical and experimental activity and paved the way toward the discovery of other interesting nondiffracting solutions [5–7]. It should be noted that even though at first sight these propagation-invariant beams may appear dissimilar, they in fact share common characteristics. In particular, they are all generated from an appropriate conical superposition of plane waves [3–7]. Even more importantly, all these solutions are known to convey infinite power: a direct outcome of their nondiffracting nature. Of course, in practice, all these nonspreading beams are normally truncated by an aperture (because of lack of space and power) and as such they tend to diffract slightly during propagation [10]. Yet, if the geometrical size of the limiting aperture greatly exceeds the spatial features of the ideal propagation-invariant fields, the diffraction process is considerably "slowed down" over the intended propagation distance and hence for all practical purposes these beams are called "diffraction-free" [11]. It should be emphasized that no localized 1D propagation-invariant beam can be synthesized through conical superposition.

Recently, a specific type of nondiffracting beams, namely, self-accelerating *Airy beams* [12, 13] has attracted a great deal of interest due to their unique properties and many potential applications such as in optical micromanipulation [14–16], plasma guidance [17, 18], vacuum electron acceleration [19, 20], and routing surface plasmon polaritons [21]. In contradistinction with the Bessel beams, the Airy beams do not rely on simple conical superposition of plane waves, and they possess the properties of self-acceleration in addition to nondiffraction and self-healing. For the past few years, tremendous research work has been devoted to the study of Airy beams, from theoretical predictions to experimental observations, from linear control to nonlinear self-trapping, and from fundamental aspects to demonstrations of proposed applications.

In this chapter, we provide an overview on generation of linear and nonlinear control of Airy beams and recent developments in this area. In just a few years, driven by both fundamental interest and application potential, the number of research papers dealing with optical Airy beams has risen dramatically. Thus, we discuss only a selection of our published papers and mention a few others significant to the field. This overview is by no means all-inclusive, nor is it meant to be.

1.2 Generation of Optical Self-accelerating Airy Beams

1.2.1 Ideal Infinite-Energy Airy Beams

We begin our analysis by considering the (1 + 1)D paraxial equation of diffraction that governs the propagation dynamics of the electric field envelope φ associated with planar optical beams:

$$i\frac{\partial\varphi}{\partial\xi}+\frac{1}{2}\frac{\partial^2\varphi}{\partial s^2}=0. \tag{1.1}$$

In (1.1), $s = x/x_0$ represents a dimensionless transverse coordinate, x_0 is an arbitrary transverse scale, $\xi = z/kx_0{}^2$ is a normalized propagation distance (with respect to the Rayleigh range), and $k = 2\pi n/\lambda_0$ is the wave number of the optical wave. Incidentally, this same equation is also known to govern pulse propagation in dispersive media.

As first shown in [1], (1.1) admits the following Airy nondispersive solution:

$$\varphi(s,\xi)=\mathrm{Ai}\left[s-\left(\frac{\xi}{2}\right)^2\right]\exp\left(is\frac{\xi}{2}-\frac{i\xi^3}{12}\right). \tag{1.2}$$

Clearly, at the origin $\varphi(s, 0) = \mathrm{Ai}(s)$, (1.2) shows that the intensity profile of this wave remains invariant during propagation while it experiences constant *transverse acceleration*. The term $(\xi/2)^2$ in (1.2) describes this ballistic trajectory. Figure 1.1 depicts the diffraction-free propagation of such an accelerating Airy wave packet as a function of distance ξ. An alternative interpretation of this interesting result was given by Greenberger through the principle of equivalence [22]. More specifically, he remarked that a stationary Airy wave packet associated with a quantum mechanical particle in a constant gravitational field will be perceived as accelerating upwards by a free-falling

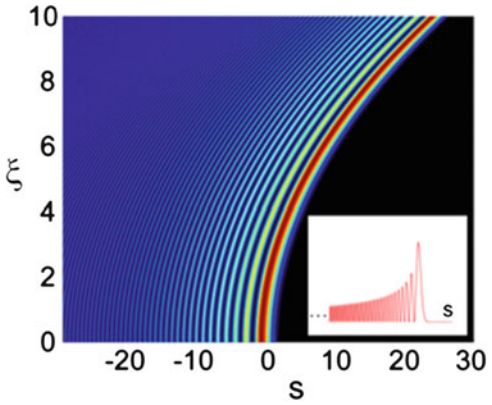

Fig. 1.1 Propagation dynamics of a diffraction-free Airy wave. The corresponding input intensity of the beam is shown in the *inset*

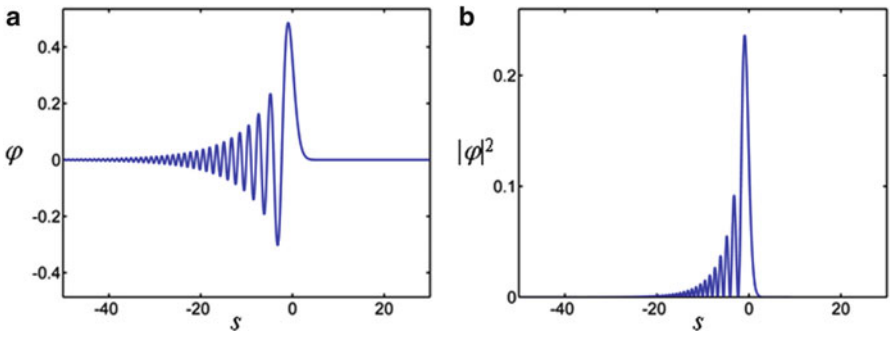

Fig. 1.2 Normalized field profile (**a**) and intensity profile (**b**) of a finite-energy Airy beam when $\alpha = 0.1$

observer in whose frame of inertia gravitational forces are absent. As also indicated in [1], this accelerating behavior is by no means in conflict with Ehrenfest's theorem which describes the motion of the center of gravity of a wave packet [1, 9]. This is simply because the Airy beam is not square integrable ($\int \mathrm{Ai}^2(x)\mathrm{d}x \to \infty$), and thus, its center of mass cannot be defined [1, 23]. Note that, ideally, the Airy beam would have infinite energy, thus it keeps the transverse acceleration and diffraction-free propagation no matter how far it travels, much like a free-falling object that always keeps the gravitational acceleration in absence of friction or obstacles.

1.2.2 Truncated 1D and 2D Airy Beams: Theory

Infinite-energy Airy beams are impossible in practice. One possible way to realize such beams is to introduce an exponential aperture function, i.e., let

$$\varphi(s, 0) = \mathrm{Ai}(s)\ \exp(\alpha s) \tag{1.3}$$

at the input of the system ($\xi = 0$). In (1.3) the decay factor $\alpha > 0$ is a positive quantity so as to ensure containment of the infinite Airy tail and can thus enable the physical realization of such beams. Note that the positive branch of the Airy function decays very rapidly and thus the convergence of the function in (1.3) is guaranteed. Figure 1.2a depicts the field profile of such a truncated Airy beam at $\xi = 0$, whereas Fig. 1.2b plots its corresponding intensity.

Of particular interest is the Fourier spectrum of this beam which in the normalized k-space is given by:

$$\Phi_0(k) = \exp(-\alpha k^2)\ \exp\left(\frac{i}{3}(k^3 - 3\alpha^2 k - i\alpha^3)\right). \tag{1.4}$$

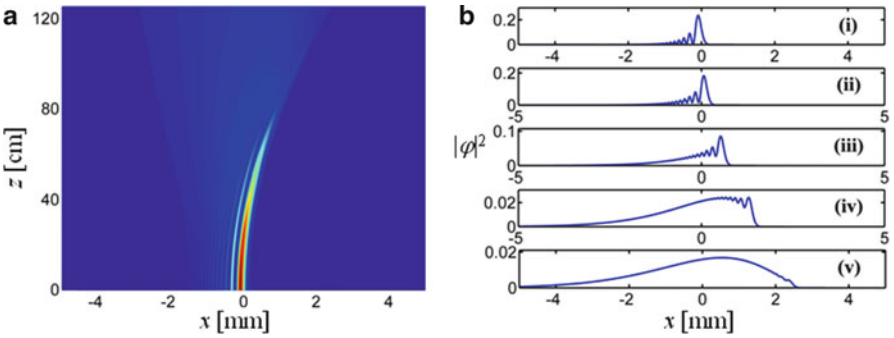

Fig. 1.3 (**a**) Propagation dynamics of a finite-energy Airy beam as a function of distance, (**b**) cross sections of the normalized beam intensity at (i) $z = 0$ cm, (ii) 31.4 cm, (iii) 62.8 cm, (iv) 94.3 cm, and (v) 125.7 cm

From (1.4) it becomes directly evident that the wave packet power spectrum is Gaussian. From Parseval's theorem, the total power of this finite-energy Airy wave packet can be directly obtained and is given by:

$$\int_{-\infty}^{\infty} \mathrm{d}s|\varphi(s,\xi=0)|^2 = \sqrt{\frac{1}{8\pi\alpha}}\exp\left(\frac{2\alpha^3}{3}\right). \tag{1.5}$$

By directly solving (1.1) under the initial conditions of (1.3), we find that the Airy beam evolves according to:

$$\varphi(s,\xi) = \mathrm{Ai}\left[s-\left(\frac{\xi}{2}\right)^2 + i\alpha\xi\right]\exp\left(\alpha s - \frac{\alpha\xi^2}{2} - \frac{i\xi^3}{12} + i\alpha^2\frac{\xi}{2} + is\frac{\xi}{2}\right). \tag{1.6}$$

Note that in the limit $\alpha = 0$ our solution reduces to the nondispersive wave packet shown in (1.2). Figure 1.3a shows the propagation of such a planar Airy beam up to a distance of 1.25 m when $x_0 = 100$ μm and the decay parameter is $\alpha = 0.1$. The corresponding cross sections of the intensity profiles at various distances are shown in Fig. 1.3b. For these parameters, the intensity FWHM of the first lobe of this beam is 171 μm. We note that for a Gaussian beam of this same width, its Rayleigh range would have been 13.25 cm at a wavelength of $\lambda_0 = 0.5$ μm. For this example, the intensity features of this beam remain essentially invariant up to 75 cm as clearly seen in Fig. 1.3. Evidently this wave endures because of the quasi-diffraction free character of the Airy wave packet. We emphasize that for this same distance, the front lobe of the beam would have expanded by at least six times. As illustrated in Fig. 1.3b, the beam starts to deteriorate first from the tail as a result of truncation. The last feature to disappear (around 100 cm) is the front lobe. After a certain distance (in this case 120 cm), the beam intensity becomes Gaussian-like, i.e., as expected from its Gaussian power spectrum in the Fraunhofer limit.

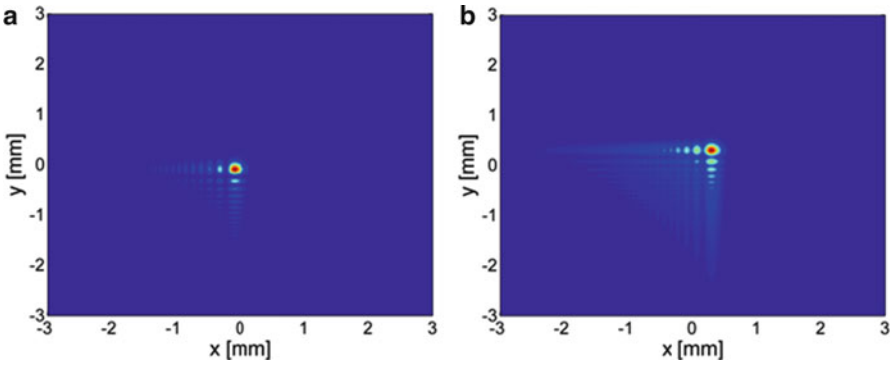

Fig. 1.4 A two-dimensional finite-energy Airy beam at the input $z = 0$ (**a**) and after propagating to $z = 50$ cm (**b**)

Even more importantly, in spite of its truncation (necessary for its realization), the Airy wave packet still exhibits its most exotic feature, i.e., its trend to freely accelerate. This characteristic is rather peculiar given the fact that it may occur in free space, e.g., in the absence of any index gradients such as from prisms or layered media. This behavior is reflected in the term $s - (\xi/2)^2$ that appears in the argument of the Airy function in (1.6). These acceleration dynamics can be clearly seen in Fig. 1.3a, where the beam's parabolic trajectory becomes evident. For the example discussed here, the beam will shift by 880 μm at $z = 75.4$ cm [12].

These results can be readily generalized into 2D domain, i.e., when the initial field envelope is given by

$$\varphi(x, y, z = 0) = \mathrm{Ai}\left(\frac{x}{x_0}\right)\mathrm{Ai}\left(\frac{y}{y_0}\right)\exp\left(\frac{x}{w_1}\right)\exp\left(\frac{y}{w_2}\right). \tag{1.7}$$

The intensity profile of such a 2D beam at $z = 0$ and $z = 50$ cm is shown in Fig. 1.4a, b when $x_0 = y_0 = 100$ μm and $w_1 = w_2 = 1$ mm. In this case, the 2D Airy beam remains almost invariant up to a distance of $z = 50$ cm along the longitudinal direction while accelerating in the same manner along the 45° axis in the x–y transverse direction. This again suggests that experimental realization of finite-energy Airy beams is possible simply by truncation.

1.2.3 Truncated 1D and 2D Airy Beams: Experiment

From (1.4), one can readily deduce that the angular Fourier spectrum of the truncated Airy beam is Gaussian and involves a cubic phase (k^3) resulting from the Fourier transform of the Airy function itself. This particular form of the spectrum has important implications in terms of experimental synthesis of

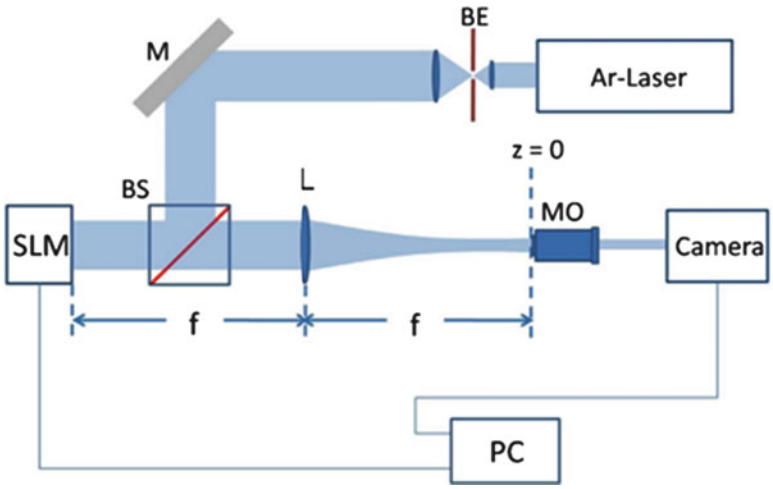

Fig. 1.5 Experimental setup for generation of truncated Airy beams. *SLM* spatial light modulator, *BE* beam expander, *MO* microscope objective

the truncated version of Airy packets. As a result, this wave can be generated from a broad Gaussian beam through a Fourier transformation provided that a cubic phase is imposed. Experimentally, such a cubic phase can be readily realized with Gaussian laser beam by using a spatial light modulator (SLM).

A typical experimental setup for Airy beam generation is illustrated in Fig. 1.5. An air-cooled Argon-ion continuous-wave laser operating at 488 nm emits a linearly polarized fundamental Gaussian beam that is subsequently collimated to a width of 6.7 mm (FWHM). This broad Gaussian beam is then reflected from the front facet of a computer-controlled liquid crystal SLM. The SLM is used to impose the cubic-phase modulation (from -20π to 20π in 2 cm) that is necessary to produce the Airy beam. In order to generate a 1D (or 2D) Airy beam, a converging cylindrical (or circular) lens with a focal length of $f = 1.2$ m is placed at a distance f in front of the SLM phase array. After the SLM, the Fourier transform of the phase-modulated Gaussian beam is then obtained at a distance $d = f = 1.2$ m behind the lens. The Airy beam produced is then imaged on a carefully aligned CCD camera through a $5\times$ microscope objective. The propagation of the Airy beam is then monitored by translating the imaging apparatus. Figure 1.6a, b shows the phase masks used to generate the 1D and 2D Airy beams, respectively.

Experimental results of a 1D Airy beam propagation in free-space are shown in Fig. 1.7, where Fig. 1.7a depicts the intensity profile of the 1D exponentially truncated Airy beam at the origin ($z = 0$). In our experiment, $x_0 = 53$ μm and $\alpha = 0.11$. Figure 1.7b, c shows the corresponding intensity profiles of this Airy packet at $z = 10$, 20 cm, respectively. As expected, the beam remains almost diffraction-free while its main lobe tends to quadratically accelerate. Our measurements show that the spatial FWHM width of the main lobe (containing

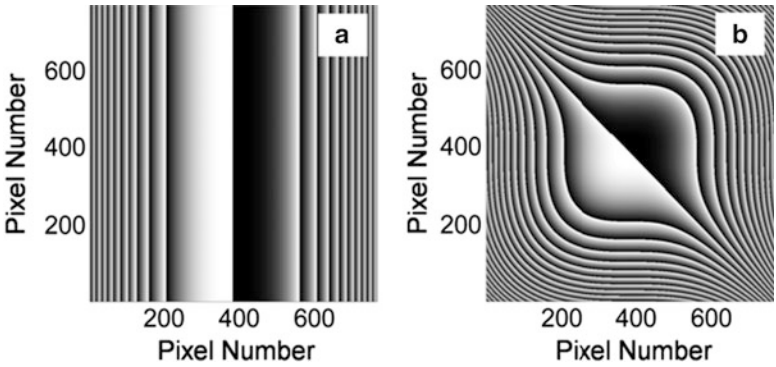

Fig. 1.6 Phase masks used to generate (**a**) 1D and (**b**) 2D-Airy beams. The cubic phase is "wrapped" between $[0, 2\pi]$. In the gray-scale pattern, *black* corresponds to 0 and *white* to 2π radians

in this case more than 70% of the total beam energy) remains almost invariant up to a distance of approximately 25 cm and retains its original value of ≈90 μm. It is worth noting that this occurs in free space and is by no means a result of any optical nonlinearity [24]. Figure 1.7d–f depicts the corresponding expected theoretical behavior of this same Airy packet at these same distances in good agreement with the experiment. Note that a Gaussian beam of this size would have diffracted at least 6–7 times in this same distance, shown in Fig. 1.7g, h.

Our experiment also demonstrated the transverse acceleration of the local intensity maxima, shown in Fig. 1.8. This parabolic-like trajectory is a result of acceleration and is well described by the theoretical relation $x_d = \lambda_0^2 z^2/(16\pi^2 x_0^3)$, as long as the beam remains quasi-diffraction free and before diffraction effects take over. The solid line in Fig. 1.8 corresponds to the latter analytical expression. As these results indicate, after 30 cm of propagation the beam experiences a deflection of 820 μm comparable to the total size of the packet (≈first 10 lobes of the Airy beam). Again, we emphasize that the acceleration observed here refers to the local intensity features of the packet. In all cases, the center of gravity $\langle x \rangle$ of this wave remains invariant [1, 25] since $\mathrm{d}\langle x \rangle/\mathrm{d}z \propto (i/2)\int(\varphi_x{}^*\varphi - \varphi_x\varphi^*)\mathrm{d}x$ is constant.

Similarly we have also considered 2D Airy beams. The case of an ideal 2D Airy packet was first suggested by Besieris et al. [26]. In this case a 2D SLM phase pattern (Fig. 1.6b) was imposed on the Gaussian beam and was then Fourier transformed through a spherical lens. By doing so we were able to produce finite energy Airy wave packets of the form in the right side of (1.7). The evolution diffraction dynamics of the latter 2D field configurations can be readily solved by separation of variables using the result of (1.6). The intensity distribution of such a wave is shown in Fig. 1.9a, when $w_1 = w_2$, corresponding to an x–y truncation factor of $\alpha = 0.11$. In this case, approximately 50% of the energy resides in the main intensity lobe at the corner. In general, the flexibility in separately adjusting the x–y parameters allows one to control the transverse acceleration vector of this novel 2D nondiffracting beam. In our

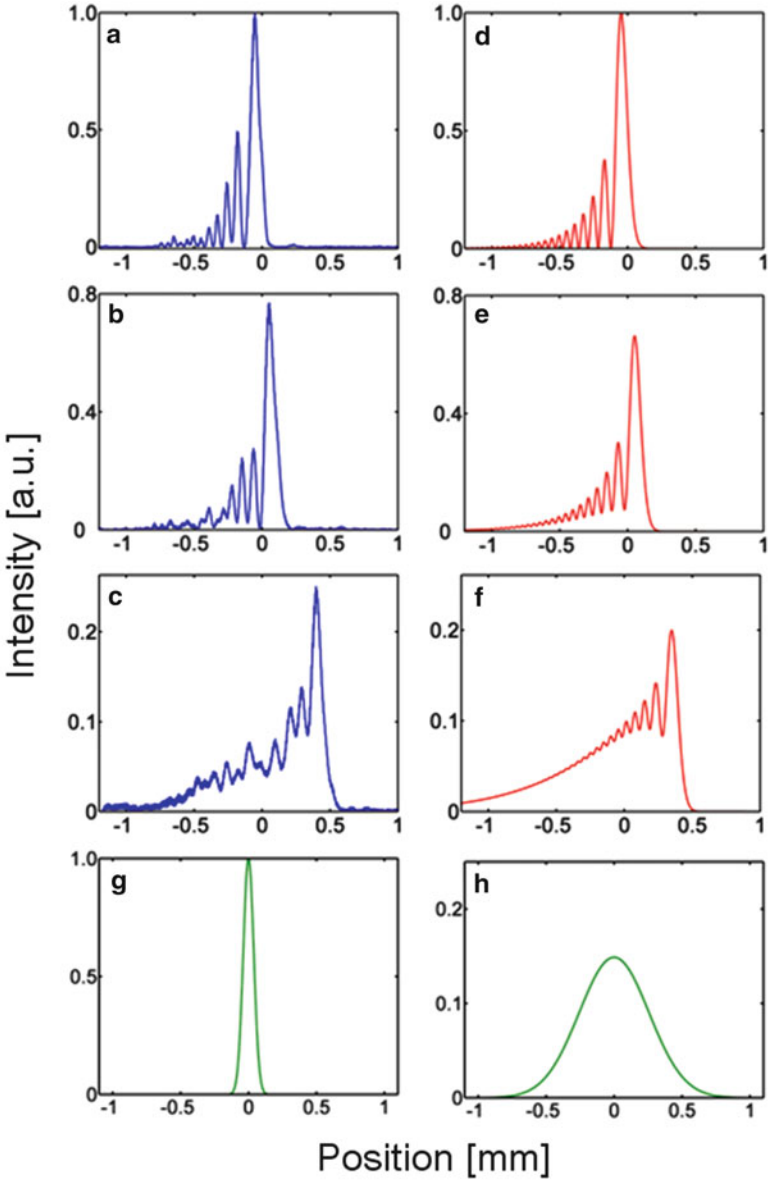

Fig. 1.7 Observed intensity cross sections of a planar Airy beam at (**a**) $z = 0$ cm, (**b**) 10 cm, and (**c**) 20 cm. Corresponding theoretical plots for these same distances (**d**), (**e**) and (**f**). (**g** and **h**) represent a comparison with a Gaussian beam having the same FWHM as the first lobe of the Airy beam

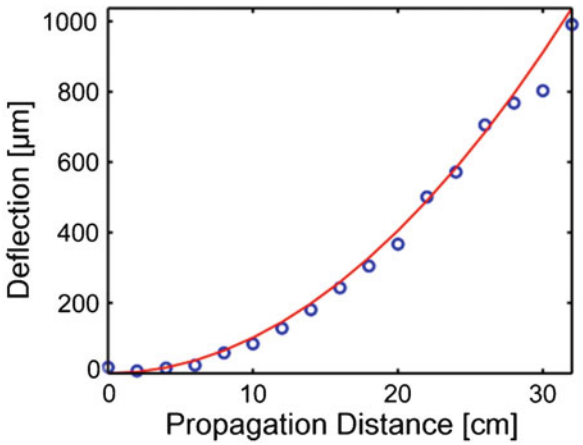

Fig. 1.8 Transverse acceleration of an Airy beam when $\alpha = 0.11$ as a function of distance. *Circles* mark experimental results while the *solid line* represents the expected theoretical deflection

experiments we considered beams with equal scales in x–y, and thus the acceleration occurred along the 45° axis. For the pattern generated, $x_0 = 53$ μm and the aperture factor is $\alpha = 0.11$. As in the 1D case, our experimental results indicate that this 2D beam propagates almost diffraction-free up to a distance of 25 cm. The main lobe keeps its spot-size (90 μm) up to a distance of ~25 cm and the beam moves on a 2D parabolic trajectory with $x_d = y_d$. The propagation and diffraction dynamics of these 2D Airy beams is shown in Fig. 1.9b–g [13].

Up to now, many different methods have been developed to generate Airy beams. As an alternative of cubic phase mask, 3/2 phase [27] or binary phase mask [28] can be explored; besides using SLM, Airy beams can also be implemented through nonlinear processing [29] or assembly of lenses [30]. In addition, Airy beams can be the direct output of a microchip laser [31].

1.2.4 Spatiotemporal Airy–Bessel Bullets

We point out that, since the Airy beams are the only type of nondiffracting wave packets found so far that exist in 1D form, they can also be synthesized in the temporal domain using dispersive elements [32]. This could lead to, for example, the observation of dispersion-free Airy pulses in optical fibers, in both the normal and anomalous dispersion regime [33]. This unique character distinguishes the Airy beams from other diffraction free beams, such as Bessel beams, Mathieu beams, etc., which have only the profile in 2D form.

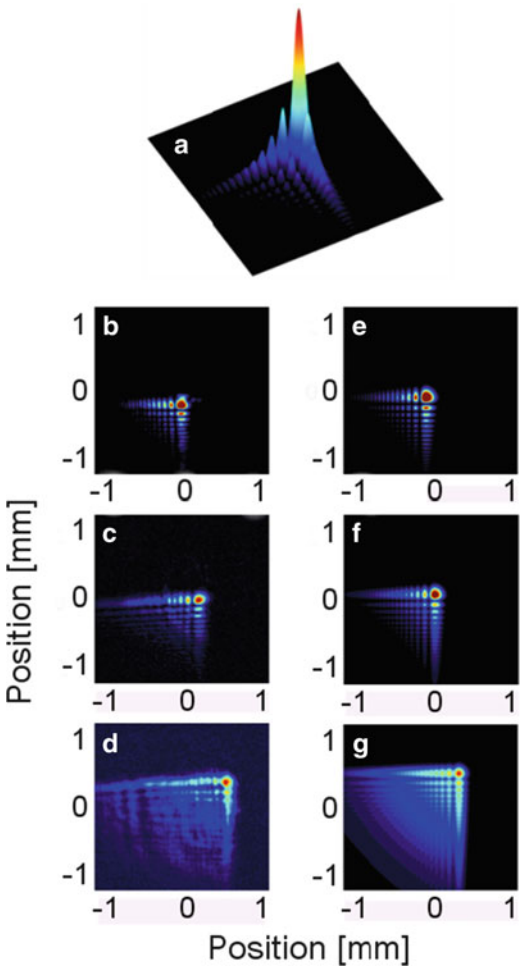

Fig. 1.9 (**a**) A schematic of a 2D Airy packet. Observed intensity distribution of a 2D Airy beam at (**b**) $z = 0$ cm, (**c**) 10 cm, and (**d**) 20 cm. Corresponding theoretical results at these same distances (**e**), (**f**), and (**g**)

Theoretically, the Airy beams in combination with other nondiffracting field configurations can also be used to describe multidimensional [(3 + 1)D] finite energy wave packets in the presence of diffraction and dispersion. In such a case, the beam envelope in the spatiotemporal domain obeys [34]:

$$i\frac{\partial \Psi}{\partial Z} + \frac{1}{2}\left(\frac{\partial^2 \Psi}{\partial X^2} + \frac{\partial^2 \Psi}{\partial Y^2} + \frac{\partial^2 \Psi}{\partial T^2}\right) = 0, \tag{1.8}$$

where in (1.8), without any loss of generality, an anomalously dispersive system was assumed. For example, a localized Airy finite energy spatiotemporal wave

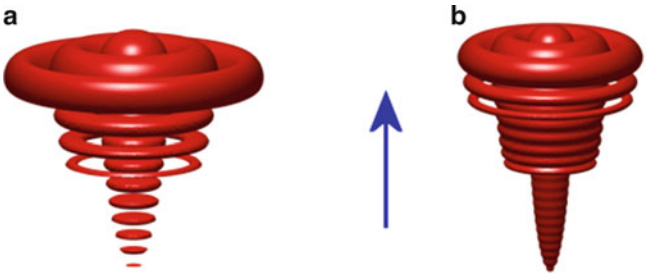

Fig. 1.10 Isosurface intensity contour plot for a spatiotemporal Airy–Gauss–Bessel wave packet (with $\alpha = 0.15$, $w_0 = 9$) (**a**) at the input $Z = 0$ and (**b**) after a normalized propagation distance of $Z = 3$. The *arrow* depicts the direction of acceleration

packet can be obtained using Bessel–Gauss beams [10], i.e., at the input $\psi = \mathrm{Ai}(T)\exp(\alpha T)J_0(r)\exp(-r^2/{w_0}^2)$, where $r = (X^2 + Y^2)^{1/2}$ and w_0 is the "aperture" spot-size of the beam. Under these initial conditions, using separation of variables we find that this wave evolves according to $\psi = \varphi(Z, T)U(Z, X, Y)$, where $\varphi(Z, T)$ is given by (1.6), and $U(Z, X, Y)$ is given by the solution of Gori et al. [10]. Figure 1.10 depicts an isosurface plot of such an Airy–Bessel–Gauss wave packet at the input $Z = 0$ and after propagation to $Z = 3$. Even in this case the wave accelerates forward and remains essentially invariant.

Accelerating Airy wave packets can also be implemented in dispersive optical fibers. Equation (1.4) suggests that in the temporal domain, such an exponentially decaying Airy pulse can be produced by passing a transform limited Gaussian pulse through a system with appreciable cubic dispersion [33]. A system of this sort can be implemented using another fiber at the zero dispersion point or by employing pulse shaping techniques [35]. Acceleration pulse dynamics can then be observed in a fiber with either normal or anomalous group velocity dispersion.

Recently, spatiotemporal optical wave packets impervious to both dispersion and diffraction, referred to as *light bullets*, have been investigated by a few groups. In particular, Abdollahpour et al. [36] demonstrated the realization of intense Airy–Airy–Airy (Airy^3) light bullets by combining a spatial Airy beam with an Airy pulse in time. The Airy^3 light bullets belong to a family of linear spatiotemporal wave packets and they can withstand both diffraction and dispersion during their propagation. It was shown that the Airy^3 light bullets are robust up to the high intensity regime, since they are capable of healing the nonlinearly induced distortions of their spatiotemporal profile. Chong et al. also demonstrated Airy-based light bullets as 3D linear localized waves in free space [37]. The method employed in the latter work is independent of any particular material or nonlinearity, as the wave packets were formed by combining the Bessel beams in the transverse plane with temporal Airy pulses, which can be extended in a straight manner to explore other transversely nondiffractive beams. These versatile 3D optical bullets in free space might break through the limitations brought by other methods for generation of light bullets.

1.2.5 Radially Symmetric Autofocusing Beams

Quite recently, a new class of 2D and 3D waves that tend to autofocus in an abrupt fashion has been introduced [38]. While the maximum intensity of such a radial wave remains almost constant during propagation, it suddenly increases by orders of magnitude right before its focal point. These waves can be generated through the use of radially symmetric Airy waves or by appropriately superimposing Airy wave packets.

To analyze the properties of such waves, let us first consider the Fresnel diffraction equation in cylindrical coordinates

$$iu_z + \frac{1}{2}\left(u_{rr} + \frac{1}{r}u_r\right) = 0. \tag{1.9}$$

The propagation of an arbitrary radially symmetric initial condition $u(r, z = 0) = u_0(r)$ according to (1.9) can be computed by utilizing the Hankel transform pair

$$u(r,z) = \frac{1}{2\pi}\int_0^\infty k\tilde{u}_0(k)J_0(kr)\mathrm{e}^{-ik^2z/2}\mathrm{d}k, \quad \tilde{u}_0(k) = 2\pi\int_0^\infty ru_0(r)J_0(kr)\mathrm{d}r. \tag{1.10}$$

In particular, a radially symmetric exponentially apodized Airy beam is considered as an initial condition

$$u_0(r) = \mathrm{Ai}(r_0 - r)\,\exp[\alpha(r_0 - r)], \tag{1.11}$$

where r_0 is the radius of the main Airy ring, and α is the apodization rate. The power that the Airy ring of (1.11) carries is given by

$$P = 2\pi\int_0^\infty |u_0|^2 r\,\mathrm{d}r \approx \sqrt{\frac{\pi}{2\alpha}}\,\mathrm{e}^{2\alpha^3/3}\left[r_0 + \frac{1-4\alpha^3}{4\alpha}\right], \tag{1.12}$$

where in the computation of the above integral we extended the lower integration limit to minus infinity (alternatively for the slightly modified initial condition $\mathrm{Ai}(r_0 - r)\mathrm{e}^{\alpha(r_0-r)} - \mathrm{Ai}(r - r_0)\mathrm{e}^{\alpha(r-r_0)}$ the above formula for the power becomes exact). The propagation dynamics of such an Airy ring is depicted in Fig. 1.11 [38]. Qualitatively the dynamics can be described as following: in the early stages of propagation, r_0 is large enough and the disk $r < r_0$ is essentially dark. As a result, in the region where the amplitude is large the approximation $\nabla_\perp u \approx u_{rr}$ holds, and thus the 1D Airy solution (1.6) with $s \to r - r_0$, can approximate the propagation dynamics. From (1.6), one may expect that the maximum value of the amplitude is going to slowly decrease along z. On the other hand, as z increases, the radius of the Airy beam decreases, the power concentrates in a smaller area, and the maximum amplitude increases. In fact, the numerical simulations show

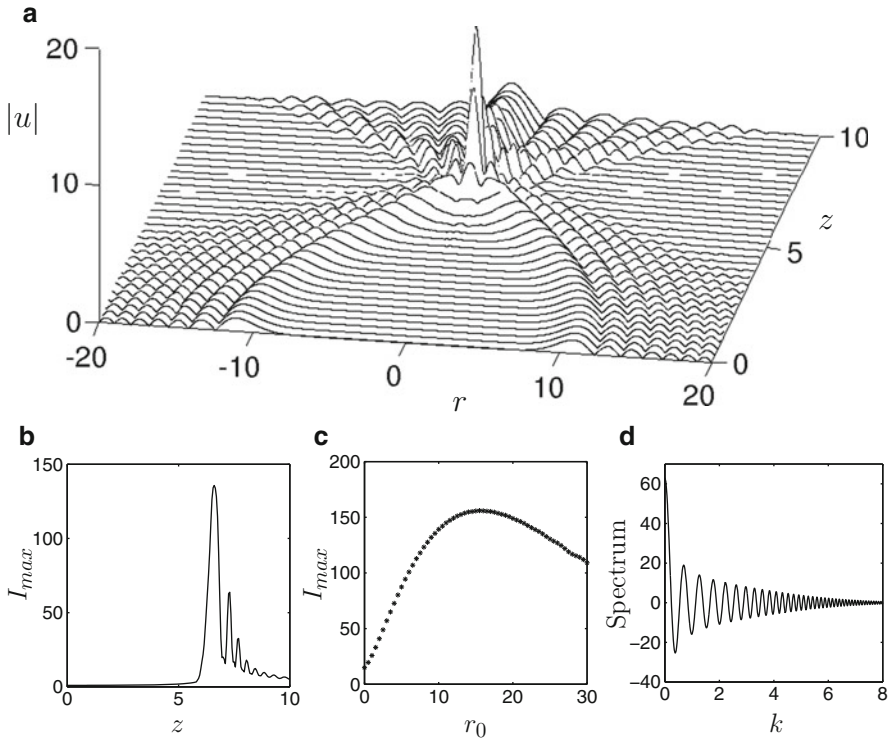

Fig. 1.11 Dynamics of radially symmetric Airy beams for $\alpha = 0.05$, $r_0 = 10$, and $I_{\max}(z = 0) = 1$; (**a**) detailed plot of the central part of the propagation dynamics; (**b**) maximum intensity as a function of z; (**c**) Maximum intensity that the Airy beam reaches during propagation for different values of the initial radius r_0; (**d**) Hankel transform of the initial condition

that these two effects almost balance each other, leading to relatively small maximum amplitude changes, up to the point where the beam reaches the center (Fig. 1.11a, b). Close to the focal point, the power of the first Airy ring is concentrated in a small area around $r = 0$ and the maximum intensity at the center rapidly increases. What is behind this very abrupt increase in intensity is the lateral acceleration of the Airy beams themselves. In this case, large transverse velocities are attained and energy rushes in an accelerated fashion toward the focus. While the peak intensity remains around unity up to $z \approx 6$, it then very rapidly increases by more than 135 times at the focal point (Fig. 1.11b). For longer propagation distances, the maximum intensity starts to decrease. As can be seen in Fig. 1.11b, this decrease is not monotonic, but it exhibits oscillations, which are generated by the subsequent Airy rings. Interestingly enough, at a final stage the solution takes the form of a Bessel function with a chirped argument.

In Fig. 1.11c, the maximum intensity that the beam reaches during propagation is shown as a function of the initial radius r_0 for $\alpha = 0.05$. For small values of r_0, the Airy beam does not carry much power and thus the maximum intensity reached is also relatively small. As the value of r_0 increases, the maximum intensity also increases

and for $r_0 \approx 15$ it takes its maximum value ($I_{\max} \approx 156$). For even larger values of r_0, diffraction becomes significant and $I_{\max}$ starts to decrease. Note that, as shown in Fig. 1.11c, large intensity contrasts are possible for a wide range of values of r_0. Much higher values of $I_{\max}$ are possible by further suppressing diffraction (decreasing α). Figure 1.11d depicts the Hankel transform of the input field profile of this beam as a function of the radial spectral component k. The transform is a real function that oscillates between positive and negative values and its envelope is decreasing with k.

Families of abruptly autofocusing beams can also be constructed by superimposing exact Airy wave solutions. If $\phi(x,z)$ is the 1D exponentially apodized Airy wave solution as given by (1.6), then we can construct, continuous or discrete, superpositions of 2D Airy waves $\phi(x',z)\phi(y',z)$ where the coordinates (x',y') are rotated and translated with respect to (x,y) $[(x',y')^T = TR(x,y)^T$, T represents a translation, and R a rotation matrix]. A particular configuration that exhibits abruptly autofocusing dynamics consists of a continuous superposition of 2D Airy waves with centers lying on a circle and each one of them propagating towards the center of the circle [38].

The above Airy families of abruptly autofocusing waves can be generalized by considering an initial condition of the form

$$u(r, z=0) = A(r)\ \sin[q(r)], \tag{1.13}$$

where $A(r)$ is the envelope function and $q(r)$ is a sublinear chirped phase

$$q(r) = \begin{cases} C(r-r_0)^{\beta}, & r \geq r_0 \\ 0, & r < r_0 \end{cases}, \tag{1.14}$$

$C > 0$ and $1 < \beta < 2$. The term sublinear stems from the fact that the phase of a linear chirp is quadratic ($\beta = 2$). Following a ray optics approach, we find that such an initial condition generates a caustic that propagates according to

$$r = r_0 - \frac{[C\beta(\beta-1)z]^{v}}{v-1}, \tag{1.15}$$

where $v = (2-\beta)^{-1}$ [39]. Note that the caustic of the Airy beam is reproduced by setting $\beta = 3/2$ resulting to the parabolic trajectory $r = r_0 - (3Cz/4)^2$. The exponent of the power law caustic can be engineered by varying the chirp coefficient. For example, for $\beta = 5/3$ the exponent of the power law caustic becomes cubic [39, 40]. In addition, different types of convex trajectories, such as exponential, are also possible [40].

Three-dimensional abruptly autofocusing waves are also possible. The corresponding anomalous dispersion paraxial equation, which is normalized such that dispersion and diffraction are equalized, is given by

$$iu_z + \frac{1}{2}(u_{xx} + u_{yy} + u_{tt}) = iu_z + \frac{1}{2}\left(u_{rr} + \frac{2}{r}u_r\right) = 0, \tag{1.16}$$

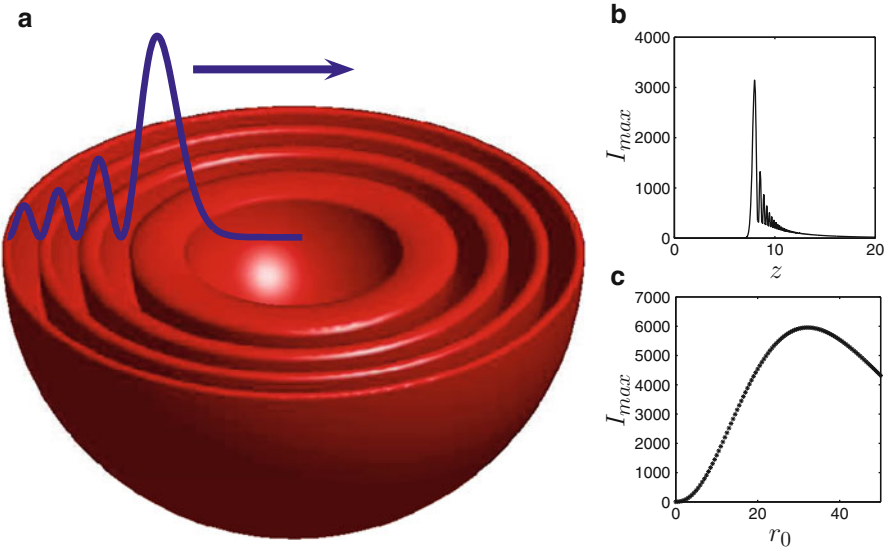

Fig. 1.12 (**a**) Isointensity hemisphere of the spherical Airy-type wave; (**b**) maximum intensity for $r_0 = 15$ as a function of z; (**c**) maximum intensity that the Airy beam reaches during propagation for different values of the radius. In (**b**), (**c**) $I_{\max}(z = 0) = 1$, $\alpha = 0.05$

where $r = \sqrt{x^2 + y^2 + t^2}$. Interestingly enough, exact expressions for the evolution of an abruptly autofocusing wave can be found in the case where the Airy beam is apodized both exponentially and with a power law r^{-1}: In this case, the solution takes the form [38]

$$u(r, z) = \frac{\phi(r_0 - r, z) - \phi(r_0 + r, z)}{r}, \tag{1.17}$$

where $\phi(x, z)$ is the 1D exponentially apodized Airy wave solution. In Fig. 1.12 dynamical properties of such a spatiotemporal wave are shown.

These radially symmetric autofocusing Airy beams have been recently generated by two research groups, along with the proposed application of such beams [15, 41, 42]. We shall discuss these applications in Sect. 1.6.4. Experimental data corresponding to the theoretical results of Fig. 1.11 are displayed in Fig. 1.13 [15]. The bottom panel shows the autofocusing beam from a side propagating view and the top panels display snapshots of transverse patterns at different propagation distances. For better visualization, the intensities in Fig. 1.13a–d have all been scaled to the same peak intensity; however, the intensity pattern without normalization would illustrate the drastic increase of peak intensity near the "focal point" of the circular Airy beam. In Fig. 1.13e, the propagation length is about 3 cm and the beam size changed from 600 to 20 μm. Our findings show a good agreement between theoretical and experimental results.

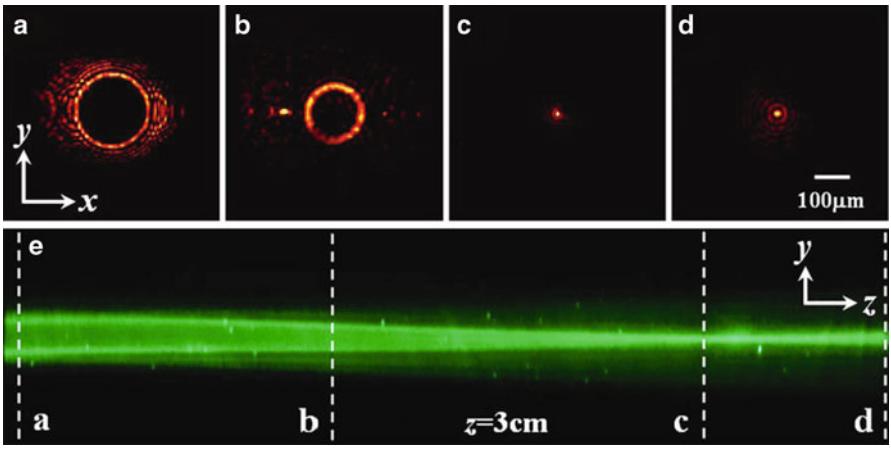

Fig. 1.13 (**a**–**d**) Experimental snapshots of transverse intensity patterns of the autofocusing beam (contrast enhanced) taken at different planes as marked in (**e**), the direct side-view photography of the beam taken from scattered light

1.3 Control of Ballistic Motion of Airy Beams

1.3.1 Ballistic Dynamics of 1D Airy Beams

The ballistic motion of optical Airy beams can be analyzed using the (1.1). In order to investigate the beam trajectories, we consider the input field distribution $\varphi(s, \xi = 0) = \mathrm{Ai}(s)\exp(\alpha s)\exp(ivs)$, where $\mathrm{Ai}(s)$ represents the Airy function, α in the exponential truncation factor is a small positive parameter, and v is associated with the initial launch angle (or "velocity") of this beam. Under these initial conditions and from (1.1), we find that this finite-energy Airy wave evolves according to:

$$\varphi(s,\xi) = \mathrm{Ai}[s - (\xi/2)^2 - v\xi + i\alpha\xi]\,\exp(\alpha s - \alpha\xi^2/2 - \alpha v\xi) \times \exp\{i[-\xi^3/12 + (\alpha^2 - v^2 + s)\xi/2 + vs - v\xi^2/2)]\}. \tag{1.18}$$

From the argument of the Airy function in (1.18), one can conclude that this beam follows a ballistic trajectory in the s–ξ plane which is described by the parabola $s = v\xi + (\xi/2)^2$. In physical units, this parabolic deflection of the beam intensity features is given by $x_d = \theta z + [z^2/(4k^2x_0{}^3)]$ where the actual launch angle θ in the x–z coordinates is related to the normalized v parameter through $\theta = v/(kx_0)$. The corresponding Newtonian (kinematical) equations describing this ballistics are $d^2x/dz^2 = 1/(2k^2x_0{}^3) = g$ and $dx/dz = gz + \theta$ where g plays here the role of "gravity". The trajectories of an ideal Airy beam (without truncation) are shown in Fig. 1.14 under different launch conditions, corresponding to three distinct regimes. More specifically, when this wave is launched upwards (when the launch angle is

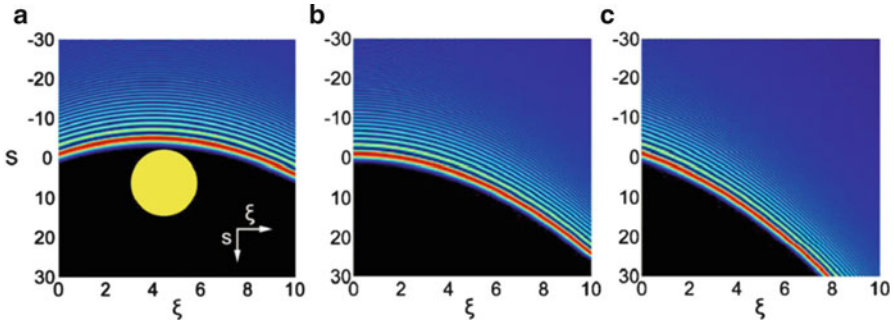

Fig. 1.14 Ballistic dynamics of an ideal Airy beam $\alpha = 0$ when (**a**) $v = -2$, (**b**) $v = 0$, and (**c**) $v = +2$. The *circle* in (**a**) represents an opaque obstacle

negative $v < 0$), the beam will initially ascend until it stalls due to downward acceleration at $\hat{z} = -\theta/g = -2k^2{x_0}^3\theta$. At this apogee point the maximum deflection is $x_{d\max} = -\theta^2k^2{x_0}^3$. From that point on, the packet will accelerate downwards as shown in Fig. 1.14a. In fact, this ballistic behavior suggests that the Airy wave packet can circumvent an opaque object O (depicted schematically in Fig. 1.14a) lying straight in its path, by following instead a curved trajectory. If on the other hand the launch angle is zero, the wave will follow a parabolic trajectory (Fig. 1.14b), similar to that predicted and demonstrated in [1, 12, 13]. The case for $v > 0$ is shown in Fig. 1.14c.

The experimental setup used to observe the ballistic dynamics of finite energy Airy wave packets is shown in Fig. 1.5. The propagation dynamics of these beams were then recorded as a function of propagation distance by translating the imaging apparatus. The origin $z = 0$ is taken at a distance f after the lens, e.g., at the point where the exponentially truncated Airy function is Fourier generated. The launch angle θ is controlled by varying the transverse displacement of the imaging lens with respect to the axis of the system. This operation is equivalent to the shifting property of Fourier transforms [43]. The ballistic dynamics of these exponentially truncated Airy beams are shown in Fig. 1.15 for various launch angles [44]. The parabolic trajectories of the intensity features of these waves were monitored up to a distance of 25 cm and the wavefront tilt angle varied from −1.33 to 0.83 mrad in order to realize the three ballistic regimes discussed above. The curves A, B, C in Fig. 1.15 were obtained for $\theta = -1.33, -1.0, -0.5$ mrad respectively. As one can clearly see, for a lunch angle of $\theta = -1.33$ mrad, the Airy beam reaches its apogee at $\hat{z} = -2k^2{x_0}^3\theta \approx 9$ cm, at which point the beam deflection is $x_{d\max} = -\theta^2k^2{x_0}^3$ ≈ 60 μm, in excellent agreement with our predictions. Curve D in Fig. 1.15 corresponds approximately to a zero launch angle. On the other hand, curve E, in Fig. 1.15, is obtained for $\theta = +0.83$ mrad. For the latter scenario, the acceleration displacement is further enhanced because of downward motion. The solid lines in Fig. 1.15 correspond to the theoretical curves associated with these cases.

Following the analysis of [1, 25], the motion of the center of gravity of these finite energy Airy wave packets can be studied. As usual, the intensity centroid is

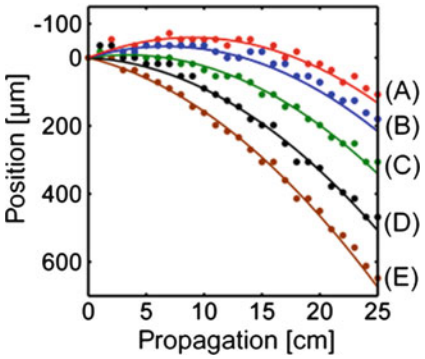

Fig. 1.15 Experimental results of Airy beam ballistics for (A) $\theta = -1.33$ mrad, (B) -1.0 mrad, (C) -0.5 mrad, (D) $+0.17$ mrad, and (E) $+0.83$ mrad

defined as $\langle s(\xi)\rangle = (1/N)\int s\left|\varphi(s,\xi)\right|^2 ds$ where in our case the constant norm is given by $N = \int\left|\varphi\right|^2 ds = (8\pi\alpha)^{-1/2}\exp(2\alpha^3/3)$. From Ehrenfest's theorem [9] it can be shown that $d\langle s\rangle/d\xi = v$, from where one can deduce that [25]:

$$\langle s\rangle = v\xi + \frac{4\alpha^3 - 1}{4\alpha}. \tag{1.19}$$

Equation (1.19) indicates that the center of gravity of these beams moves at a constant velocity (or remains invariant for $v = 0$) as a function of propagation distance. Indeed, experimental results clearly show this linear behavior for the same launch angles used in Fig. 1.15 [44]. Thus, we emphasize again that the aforementioned acceleration behavior refers to the trajectories of the local beam intensity features and is by no means in contradiction with Ehrenfest's theorem.

1.3.2 Ballistic Dynamics of 2D Airy Beams

To analyze the ballistic dynamics of 2D Airy beams, the normalized (2 + 1)D paraxial equation of diffraction is employed:

$$i\frac{\partial\varphi}{\partial z} + \frac{1}{2k}\frac{\partial^2\varphi}{\partial x^2} + \frac{1}{2k}\frac{\partial^2\varphi}{\partial y^2} = 0, \tag{1.20}$$

where φ is the electric field envelope and $k = 2\pi n/\lambda_0$ is the wavenumber of the optical wave. The evolution of a 2D finite energy accelerating Airy beam, whose field profile at the origin is given by $\varphi(x,y,z=0) = \prod_{m=x,y}\mathrm{Ai}(s_m)\exp(\alpha s_m)\exp(iv_m s_m)$, can be obtained in closed form:

$$\varphi(x,y,z) = \prod_{m=x,y} u_m(s_m,\xi_m), \tag{1.21}$$

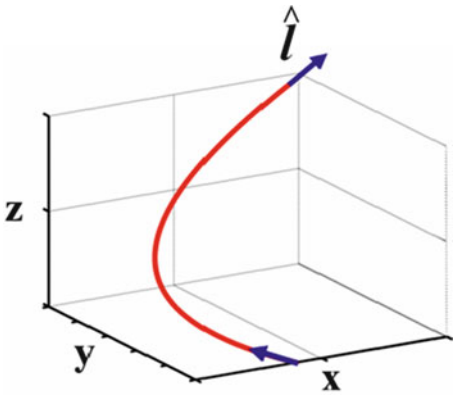

Fig. 1.16 Motion of the main lobe of a symmetric ($x_0 = y_0 = 77$ μm) 2D Airy beam when launched at $\theta_x = -2$ mrad and $\theta_y = 2$ mrad

where

$$u_m(s_m, \xi_m) = \mathrm{Ai}[s_m - (\xi_m/2)^2 - v_m\xi_m + i\alpha_m\xi_m]\,\exp(\alpha_m s_m - \alpha_m {\xi_m}^2/2 - \alpha_m v_m \xi_m) \times \exp\{i[-{\xi_m}^3/12 + ({\alpha_m}^2 - {v_m}^2 + s_m)\xi_m/2 + v_m s_m - v_m {\xi_m}^2/2)]\}, \tag{1.22}$$

$\mathrm{Ai}(s_m)$ denotes the Airy function [23], $s_x = x/x_0$ and $s_y = y/y_0$ represent dimensionless transverse coordinates, with x_0, y_0 being arbitrary transverse scales, and $\xi_x = z/k{x_0}^2$ and $\xi_y = z/k{y_0}^2$ are used to normalize the propagation distance z. α_m in the exponential function is a small positive parameter associated with the effective aperture of the system, and v_m is related to the initial launch angle θ_m (or "velocity") of this beam through $\theta_m = v_m/k(x_0, y_0)$.

From (1.22), one can also directly determine the trajectory of the main ("head") lobe of the Airy beam as a function of distance. This 3D curve is given by:

$$x_d = \frac{1}{4k^2x_0^3}z^2 + \theta_x z$$
$$y_d = \frac{1}{4k^2y_0^3}z^2 + \theta_y z\,. \tag{1.23}$$

In principle this trajectory can be appropriately tailored through the magnitude and sign of the launch angles θ_m, and the scales x_0, y_0. Clearly, for zero launch angles θ_m and if $x_0 = y_0$, the main lobe of the Airy beam will move on a parabola (projected along the 45° axis in the x–y plane). On the other hand, a "boomerang-like" curve may be created if for example the "launch" angles are chosen to have opposite signs, say $\theta_x = -2$ mrad and $\theta_y = 2$ mrad (while $x_0 = y_0 = 77$ μm), as shown in Fig. 1.16. What is also very interesting is the fact that these displacements vary quadratically with the wavelength λ_0.

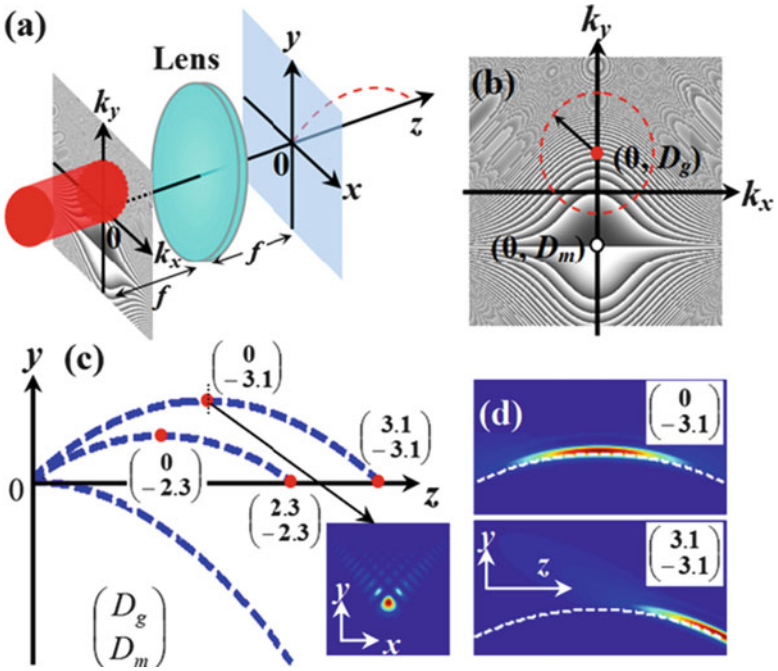

Fig. 1.17 (**a**) Schematic of input Gaussian beam, cubic phase mask, and Fourier lens used for generation of truncated Airy beam; (**b**) location of mask (center denoted by *white spot*) and input beam (marked by *red dashed circle* and center denoted by *red spot*) in Fourier plane; (**c**) illustration of different trajectories obtained at different D_g and D_m when the peak beam intensity appears at maximum heights or ranges (marked by *red spots*). The inset shows the Airy beam profile at the maximum height of upper curve. The lower curve corresponds to normal excitation at $D_g = D_m = 0$, so its peak intensity is at the starting point ($z = 0$); (**d**) Numerical simulations of beam propagation for two specific cases corresponding to the upper trajectory shown in (**c**)

1.3.3 Optimal Control of the Ballistic Motion of Airy Beams

Let us consider a typical optical system for generation of 2D Airy beams as depicted in Fig. 1.17a, where a Gaussian beam is first modulated by a cubic phase mask and then passes through a Fourier transform lens. Usually, the Gaussian beam, the mask, and the Fourier lens are set to be coaxial along z. If the lens is transversely shifted, a tilting angle will be introduced into the Airy beam. As an example, let us fix the position of the lens but allow the mask and Gaussian beam to have transverse displacements in the Fourier plane. To understand the influence of these displacements, let us first consider the 1D case. The Fourier spectrum of a truncated Airy beam can be expressed as $\exp(-\alpha w^2)\ \exp[i(w^3 - 3\alpha^2 w - i\alpha^3)/3]$, where α is a small parameter for the exponential truncation factor, and w is the normalized wave number. If the Gaussian beam and the phase mask are translated by w_g and w_m in the

Fourier plane, the resulting spectrum $\exp[-\alpha(w - w_g)^2] \exp\{i[(w - w_m)^3 - 3\alpha^2(w - w_m) - i\alpha^3]/3\}$ leads to a new truncated Airy beam with a field envelope ϕ expressed as follows:

$$\phi = Cf(s,\xi)\mathrm{Ai}[s - w_m\xi - (\xi/2)^2 + i\alpha(\xi - 2w_g + 2w_m)] \exp(iw_m s), \tag{1.24a}$$

$$C = \exp(-\alpha {w_g}^2 - \alpha {w_m}^2 + i2\alpha^2 w_m - i2\alpha^2 w_g + 2\alpha w_m w_g), \tag{1.24b}$$

$$\begin{aligned} f(s,\xi) = \exp[\alpha s + is\xi/2 + (-i{w_m}^2/2 + i\alpha^2/2 - 2\alpha w_m + \alpha w_g)\xi \\ + (-\alpha/2 - iw_m/2)\xi^2 - i\xi^3/12], \end{aligned} \tag{1.24c}$$

where Ai represents the Airy function, and s and ξ are normalized transverse and longitudinal coordinates. From (1.24a), we see that the trajectory changes due to the translation of the mask as expressed by $s = w_m\xi + (\xi/2)^2$. The term $i\alpha(\xi - 2w_g + 2w_m)$ shows that the new peak-intensity position is at $\xi = 2(w_g - w_m)$, controlled by translation of both the mask and the Gaussian beam. Similar analyses can be employed for the 2D case shown in Fig. 1.17b, and the trajectory can now be expressed as $-\sqrt{2}[D_m\xi/\sqrt{2} + (\xi/2)^2]$ with a new peak-intensity position at $\xi = -\sqrt{2}D_m + \sqrt{2}D_g$ (D_g and D_m are normalized vertical displacements of the Gaussian beam and the mask in Fourier plane, respectively). Therefore, by translating the mask and Gaussian beam with respect to z-axis, the location of peak beam intensity as well as maximum height and range of the trajectory can be controlled with ease. Typical 2D numerical results are shown in Fig. 1.17c, d. For $D_g = D_m = 0$, the Airy beam propagates akin to a body projected horizontally with the peak intensity appearing at the starting point. Moving the mask to different vertical positions ($D_m \approx -2.3, -3.1$) leads to propagation of the Airy beam in a ballistic trajectory as does a batted baseball. In the case of $D_g = 0$, the peak intensity always appears at the maximum height. However, by translating also the Gaussian beam so that $D_g = -D_m$, the peak intensity appears at the maximum range ("point of fall") as demonstrated below.

Experimental results corresponding to above analyses are shown in Fig. 1.18, where a Gaussian beam is turned into a truncated Airy beam assisted with a SLM and a Fourier transform lens as shown in Fig. 1.18a. When the beam, mask, and lens are aligned coaxially, a "horizontally projected" Airy beam is generated with a decaying intensity (due to diffraction) during propagation (Fig. 1.18a). If the mask is translated slightly in vertical direction, the resulting Airy beam propagates in general ballistic trajectories with different ranges (Fig. 1.18b, d) while its peak intensity appears at the maximum heights. These different trajectories correspond to different launching angles due to the transverse displacement of the phase mask relative to the z-axis of the system. By also translating the Gaussian beam the same distance but to the opposite direction, the trajectory remains the same but the peak intensity moves to the maximum range (Fig. 1.18c, e). These experimental results agree well with our theoretical predications.

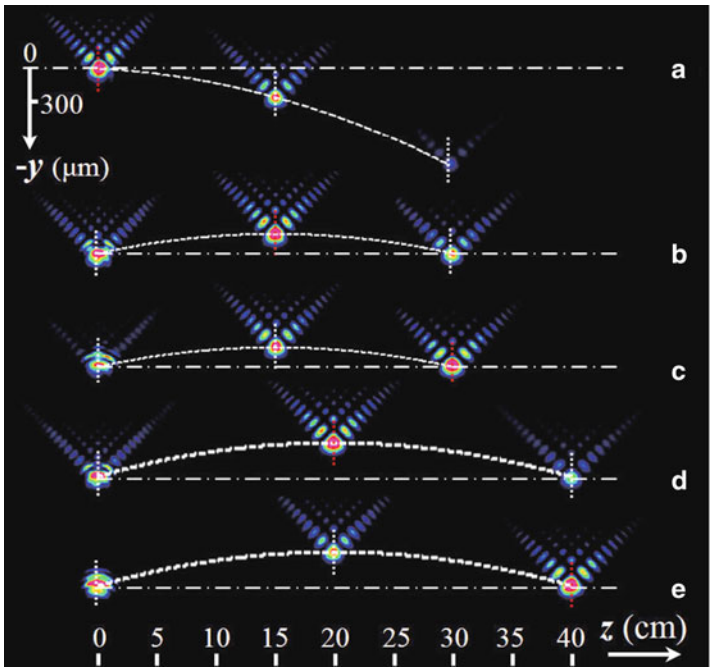

Fig. 1.18 Experimental demonstration of controlled trajectories (*white dashed curves*) of truncated Airy beams under different excitation conditions. Snapshots of transverse intensity patterns are shown at marked positions. (**a**) Normal condition when peak beam intensity is at the starting point, corresponding to lower curve in Fig. 1.17c; (**b**, **d**) peak intensity goes to the maximum height with shifting of only cubic phase mask; (**c**, **e**) peak intensity goes to the "point of fall" with additionally shifting of the Gaussian beam

If we allow both vertical and horizontal displacements of the phase mask [(D_{mx}, D_{my})] and the Gaussian beam [(D_{gx}, D_{gy})] as illustrated in Fig. 1.19a, the projectile motion of the Airy beam can be set into any arbitrary direction. Following similar theoretical analysis for Eqs. (1.24a, b, c), the (x, y) trajectory can be expressed as $[-D_{mx}\xi, -D_{my}\xi - \sqrt{2}(\xi/2)^2]$. Clearly, the Airy beam in this case undergoes uniform motion along horizontal direction while accelerating along vertical direction. As such, the Gaussian beam (even initially aiming along z-direction) can propagate to any off-axis location. The horizontal displacements of the mask and Gaussian beam will not change the location of the peak beam intensity, but they can change the Airy beam profile from symmetric (when $D_{mx} = D_{gx}$) to asymmetric (when $D_{mx} \neq D_{gx}$). An example of experimental results is shown in Fig. 1.19b, c. The peak intensity appears at the maximum height of the trajectory when the Gaussian beam is on axis ($D_{gx} = D_{gy} = 0$, shown in Fig. 1.19b) but moves to the "point of fall" when the beam is displaced vertically ($D_{gx} = 0, D_{gy} = -d$, shown in Fig. 1.19c). In this case, since $D_{mx} \neq D_{gx}$, the Airy beam starts with an asymmetric profile but evolves into a symmetric profile after restoring its peak intensity. These experimental observations are corroborated with numerical simulations [45].

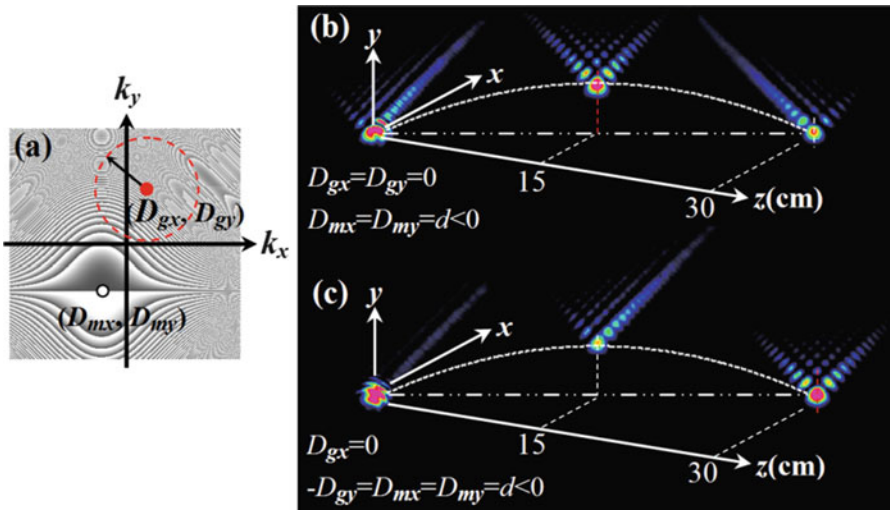

Fig. 1.19 Experimental demonstration of accelerating Airy beams with transverse uniform motion. (**a**) Relative positions of cubic phase mask and Gaussian beam in the Fourier plane; (**b**, **c**) experimental results of the trajectory and intensity pattern of the Airy beam obtained under different excitation conditions as depicted in (**a**)

1.3.4 Airy Trajectory Engineering in Dynamic Linear Index Potentials

Quite recently, we have successfully demonstrated that, with optically induced linear index potential, enhancement as well as reduction of Airy beam acceleration can be realized by changing the index gradient transversely [46]. Here we show our design of linear longitudinal (z-axis) index potential to engineer the trajectory that the Airy beam follows. In particular, let us consider the paraxial dynamics of an optical field

$$iu_z + \frac{1}{2}u_{xx} - \frac{d(z)x}{2}u = 0, \tag{1.25}$$

where $d(z)x/2$ is the transversely linear index potential with a gradient $d(z)$. In the Fourier space (1.25) becomes

$$\tilde{u}_z - \frac{d(z)}{2}\tilde{u}_k = -i\frac{k^2}{2}\tilde{u}, \tag{1.26}$$

which is equivalent to the characteristic system

$$\frac{dz}{1} = \frac{dk}{-d(z)/2} = \frac{d\tilde{u}}{-ik^2\tilde{u}/2}. \tag{1.27}$$

By integrating the above system we obtain the integral formula

$$u(x,z) = \frac{1}{2\pi}\int_{-\infty}^{\infty} \tilde{u}(k,0)\mathrm{e}^{-(i/2)\int_0^z \kappa(s)^2 \mathrm{d}s}\mathrm{e}^{i\kappa(z)x}\mathrm{d}k, \tag{1.28}$$

where $\kappa(z) = k - D(z)/2$, $D(z) = \int_0^z d(s)\mathrm{d}s$. We focus our attention on Airy type initial conditions

$$u(x, z=0) = \mathrm{Ai}(\gamma^{1/3}x), \tag{1.29}$$

where γ is the width of the Airy wave. By substituting the Fourier transform of (1.29)

$$\tilde{u}(k, z=0) = \frac{1}{\gamma^{1/3}}\exp\left[\frac{ik^3}{3\gamma}\right] \tag{1.30}$$

into (1.28) we find that

$$u(x,z) = \mathrm{e}^{\phi(x,z)}\mathrm{Ai}(\gamma^{1/3}\mu(x,z)), \tag{1.31}$$

where

$$\mu(x,z) = \frac{F_1(z)}{2} + x - \frac{\gamma z^2}{4}, \tag{1.32}$$

$$\phi = i\frac{\gamma F_1(z) z}{4} - i\frac{D(z)x}{2} - i\frac{F_2(z)}{8} + i\frac{\gamma z x}{2} - i\frac{\gamma^2 z^3}{12}, \tag{1.33}$$

and

$$F_1(z) = \int_0^z D(s)\mathrm{d}s, \quad F_2(z) = \int_0^z D^2(s)\mathrm{d}s. \tag{1.34}$$

We consider that the trajectory of the Airy beam is provided by $\mu(x,z) = 0$, i.e.,

$$x = -\frac{F_1(z)}{2} + \frac{\gamma z^2}{4}, \tag{1.35}$$

which mainly determines caustic trajectory. By generalizing the initial condition as

$$u(x, z=0) = \mathrm{Ai}(\gamma^{1/3}(x - x_0))\mathrm{e}^{i\Psi x}, \tag{1.36}$$

in which case x_0 is the initial spatial displacement and ψ is the initial tilt, the trajectory of the beam becomes

$$x = x_0 + \Psi z - \frac{F_1(z)}{2} + \frac{\gamma z^2}{4}. \tag{1.37}$$

More importantly, we can also solve the inverse problem: given a predefined Airy beam trajectory $x = g(z)$ we can determine the index gradient $d(z)$ as well as the initial condition parameters x_0, ψ that are required. Following the relevant algebra we find that

$$x_0 = g(0), \quad \Psi = g'(0), \quad d(z) = \gamma - 2g''(z). \tag{1.38}$$

In a similar fashion one can derive expressions for the dynamics of exponentially and Gaussian apodized Airy beams [47]. In particular, the trajectory of the exponentially apodized Airy beam is essentially the same as compared to the "pure" Airy beam, whereas the effective trajectory is modified in the case of a Gaussian apodization. As an example, in Fig. 1.20 we see an exponentially apodized Airy beam following different trajectories. In all cases, the potential gradient and initial condition parameters are determined by utilizing (1.38).

1.4 Self-healing of Airy Beams

1.4.1 Self-reconstructing Optical Airy Beams

Perhaps one of the most remarkable properties of any diffraction-free beam is its very ability to self-reconstruct during propagation. This characteristic is of particular importance when such waves propagate in inhomogeneous media [48]. The question naturally arises whether Airy beams can self-heal and to what extent? If so, how does this process take place and how is it affected by the beam's acceleration dynamics? For example, can an Airy beam negotiate adverse environments? In this section we review the self-healing properties of optical Airy beams. We show that this family of waves exhibits remarkable resilience against perturbations and tends to reform during propagation.

1.4.2 Babinet's Principle for a Nondiffracting Beam

The self-healing properties of a nondiffracting field configuration, when it is partially blocked by a finite opaque obstacle at $z = 0$, can be explained from Babinet's principle [49]. If the nondiffracting input field is disturbed by a finite energy perturbation $\varepsilon(x, y)$, i.e., $\varphi(x, y, z = 0) = U_{ND}(x, y, z = 0) - \varepsilon(x, y, z = 0)$, then

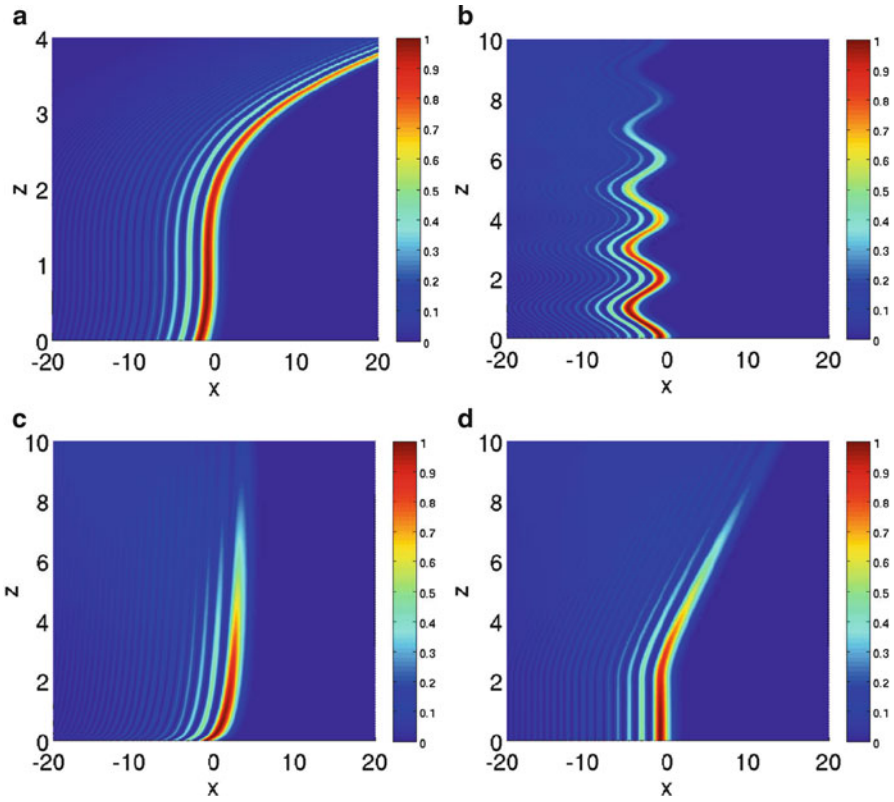

Fig. 1.20 Exponentially apodized Airy beam propagation ($\alpha = 0.05$) along predefined paths. (**a**) Power law trajectory $x = (z-1)^3$; (**b**) sinusoidal trajectory given by $x = g(z) = 2[\cos(\pi z) - 1]$; (**c**) logarithmic trajectory $x = \log(1 + 10\,z)$; (**d**) hyperbolic type trajectory given by $x = g(z) = 2[\sqrt{(z-2)^2 + 1} - 1]H(z-2)$ where $H(z)$ is the Heaviside step function

from (1.1) one finds that $i\varepsilon_z + (1/2k)\nabla_\perp^2\varepsilon = 0$. As a result the perturbation ε is expected to rapidly diffract as opposed to the nondiffracting beam that remains invariant during propagation. As a consequence, at large distances $|\varphi(x, y, z)|^2 = |U_{ND}(x, y, z)|^2$, and hence the nondiffracting beam reforms during propagation. This argument holds for all nondiffracting fields including the accelerating Airy beam.

1.4.3 Transverse Power Flow of an Optical Airy Beam

Of relevance to our discussion is the Poynting vector $\vec{S}$ associated with Airy optical beams. In the paraxial regime, $\vec{S}$ is given by [50]:

$$\vec{S} = \vec{S}_z + \vec{S}_\perp = \frac{1}{2\eta_0}|\varphi|^2\hat{z} + \frac{i}{4\eta_0 k}[\varphi\nabla_\perp\varphi^* - \varphi^*\nabla_\perp\varphi], \tag{1.39}$$

where $\eta_0 = \sqrt{\mu_0/\varepsilon_0}$ is the impedance of free space. $\vec{S}_z$ denotes the longitudinal component of the Poynting vector whereas $\vec{S}_\perp$ the transverse. From Eqs. (1.23) and (1.39) one can directly obtain the direction of the Poynting vector associated with an ideal 2D Airy ($\alpha_m = 0$) beam. More specifically, the angle ψ the projection of $\vec{S}$ makes with respect to x axis is given by:

$$\tan \Psi = \frac{S_y}{S_x} = \frac{\theta_y + \frac{z}{2k^2 y_0^3}}{\theta_x + \frac{z}{2k^2 x_0^3}}. \tag{1.40}$$

On the other hand, the direction of $\vec{S}$ relative to the z axis is given by:

$$\tan \delta = \frac{\sqrt{S_x^2 + S_y^2}}{S_z} = \sqrt{\left(\theta_x + \frac{z}{2k^2 x_0^3}\right)^2 + \left(\theta_y + \frac{z}{2k^2 y_0^3}\right)^2}. \tag{1.41}$$

Note that for ideal Airy beams, the Poynting vector $\vec{S}$ is at every point parallel to the unit tangent vector $\hat{l}$ of the trajectory curve of (1.23). This statement is also valid for finite energy Airy beams during the quasi-diffraction free stage of propagation. At larger distances, however, small deviations are expected to occur. In addition one can show that the polarization of the beam can evolve in a similar manner.

The reconstruction of an accelerating optical Airy beam can be monitored through the transverse component of the Poynting vector $\vec{S}_\perp$ [51].

1.4.4 Observation of Self-healing Properties of 2D Airy Beams

In order to study experimentally the self-healing properties of a 2D Airy beam, the Airy pattern is partially blocked in a controlled manner with a rectangular opaque obstacle inserted at the desired location, and then monitored for their self-reconstruction during propagation. In all cases we block a portion of its initial intensity profile. The most prominent intensity characteristic of an Airy beam happens to be its main corner lobe (as seen in Fig. 1.9a) which contains a large percentage of the beam's total power. In a first experiment, an opaque rectangular obstacle was employed to obstruct the corner main lobe of the Airy pattern (Fig. 1.21a). The FWHM of the blocked lobe feature was approximately 130 μm corresponding to $x_0 = y_0 = 77$ μm and $\alpha = 0.08$. Figure 1.21b depicts the reformation of this Airy beam after a distance of $z = 11$ cm. The self-healing of this beam is apparent. The main lobe is reborn at the corner and persists undistorted up to a distance of 30 cm (Fig. 1.21c). In our setup, the latter distance (30 cm) corresponds approximately to four diffraction lengths of the corner lobe. Our experimental observations are in excellent agreement with numerical results presented in Fig. 1.21d–f for the same propagation distances.

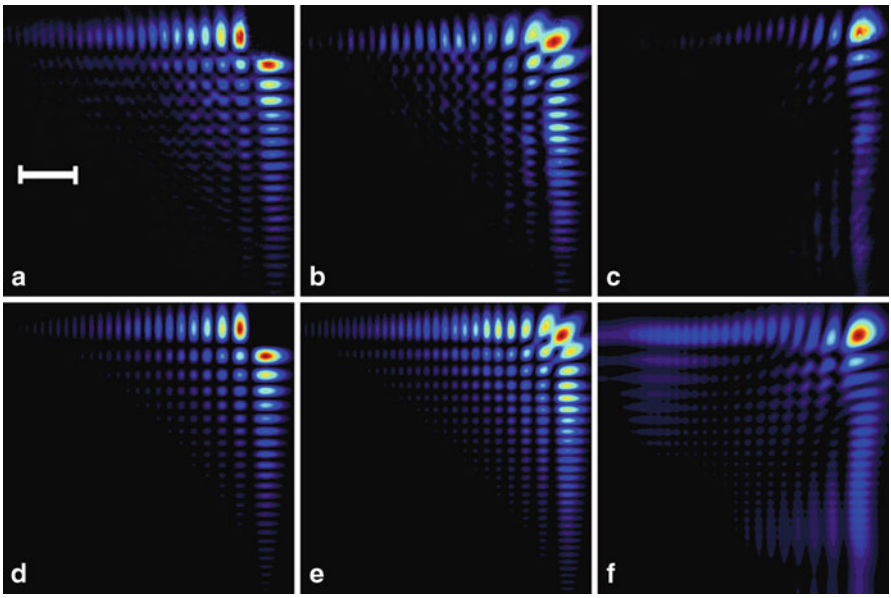

Fig. 1.21 Self-healing of an Airy beam when its main lobe is blocked. Observed intensity profile at (**a**) the input $z = 0$, (**b**) $z = 11$ cm, and (**c**) $z = 30$ cm. The corresponding numerical simulations are shown in (**d**–**f**)

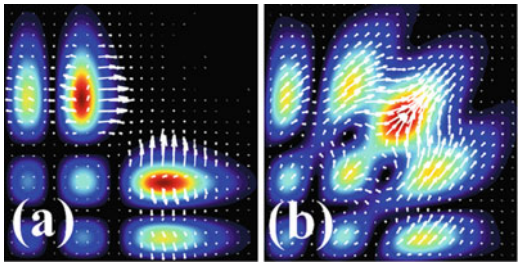

Fig. 1.22 Calculated transverse power flow $\vec{S}_\perp$ at (**a**) $z = 1$ cm and (**b**) $z = 11$ cm

We note that had the main lobe been launched in isolation it would have experienced a fivefold increase in the beam width over the same propagation distance, while the peak intensity would have dropped to 5% of its initial value. This is another manifestation of the nondiffracting nature of Airy beams.

In order to understand this self-healing process it is important to study the internal transverse power flow $\vec{S}_\perp$ within the perturbed Airy beam. To do so we use the result of (1.39). Figure 1.22a depicts the transverse flow within the Airy beam at $z = 1$ cm when the main lobe has been removed. Evidently the power flows from the side lobes towards the corner in order to facilitate self-healing. On the other hand, once

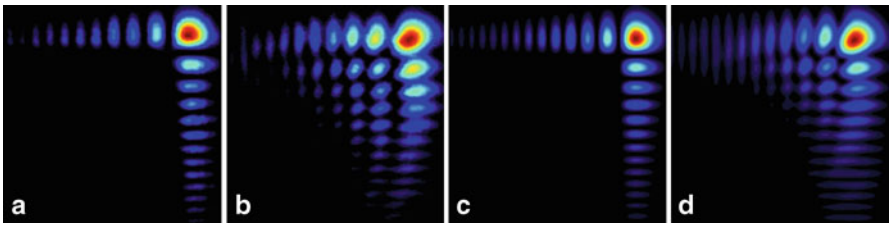

Fig. 1.23 Self-healing of an Airy beam when all the internal lobes are blocked. Observed intensity profiles at (**a**) the input $z = 0$ and (**b**) $z = 16$ cm. The corresponding numerical simulations are shown in (**c**) and (**d**)

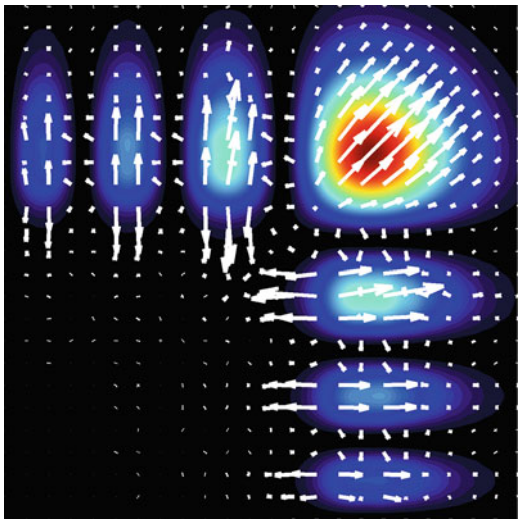

Fig. 1.24 Transverse power flow $\vec{S}_{\perp}$ revealing the self-healing mechanism at $z = 1$ cm for the incomplete Airy beam shown in Fig. 1.23

reconstruction has been reached (at $z = 11$ cm), then the internal power density around the newly formed main lobe flows along the 45° axis in the x–y plane (for $x_0 = y_0$) in order to enable the acceleration dynamics of the Airy beam (Fig. 1.22b).

So far we have experimentally demonstrated that an Airy beam can reconstruct itself when its main lobe has been blocked. It is of interest to examine whether the beam could self-heal even after more severe perturbations. In a second set of experiments we have totally blocked all the internal structure (all inner lobes) of the Airy pattern (Fig. 1.23a). Remarkably after $z = 16$ cm of propagation the beam self-heals and reconstructs in detail its fine intensity structure as depicted in Fig. 1.23b. Figure 1.23c, d shows the corresponding calculated intensity profiles for these same distances.

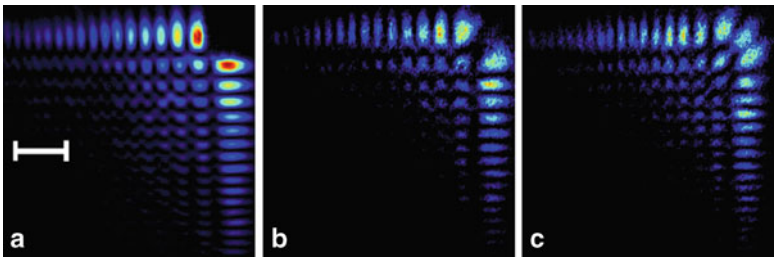

Fig. 1.25 Self-healing of an Airy beam when propagating in a suspension of 0.5 μm silica microspheres in pure water. Observed intensity profiles at (**a**) the input $z = 0$, (**b**) $z = 5$ cm, and (**c**) $z = 10$ cm

The internal power flow during the latter self-healing process is shown in Fig. 1.24. At $z = 1$ cm, the Poynting vector provides energy towards the blocked region for rebirth to occur while on the main lobe is directed along 45° in the x–y plane in order to enable the self-bending of the Airy beam.

In addition, we have also demonstrated experimentally that an Airy beam can reconstruct itself when a nonsymmetric obstruction is used. This asymmetric perturbation was carried out by blocking, for example, the first three lobes of an Airy wave packet along the y axis. Interestingly, in this physical setting, the beam not only self-heals itself but also the initially blocked part is reborn even brighter when compared to its surroundings. This is a clear manifestation of the nondiffracting character of the Airy beam [51]. In addition, this self-regeneration property can be improved by dual Airy beams [52].

1.4.5 Self-healing of Optical Airy Beams in Scattering Environments

In the previous section we have demonstrated that optical Airy beams are remarkably resilient to amplitude deformations when propagating in free space. The question is: are such self-healing Airy wave packets also robust in adverse environments? To address this question we have experimentally studied the propagation of Airy beams in scattering and turbulent media.

In order to study the self-healing dynamics of Airy beams in scattering media we have again blocked their main corner lobe (Fig. 1.25a). To do so we have prepared two different samples of silica microspheres ($n = 1.45$) suspended in pure water ($n = 1.33$). The size of the dielectric microparticles was 0.5 and 1.5 μm in diameter and thus light scattering was predominantly of the Mie type [53]. Both suspensions were 0.2% in weight concentration while the volume filling factor was 0.1%. We have ultrasonicated the prepared mixtures for 1 h, to make sure that the silica particles were monodispersedly suspended in water. The scattering cross section of the microspheres is estimated to be 0.055 and 3.76 μm^2 [54] for the small and large

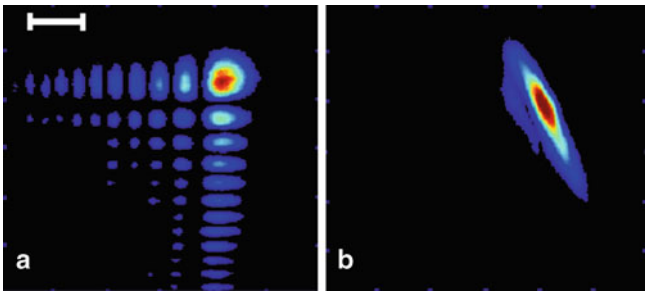

Fig. 1.26 Propagation in a turbulent medium of (**a**) an optical 2D Airy beam and (**b**) a comparable Gaussian beam

particles, respectively. These values lead to significant light scattering, enough to give a granular appearance when the beam propagates 5 cm in the water–silica mixture (diameter of 0.5 μm) (Fig. 1.25b). A longer (10 cm) cell was used to observe the complete reformation of the Airy pattern in the same scattering media. Figure 1.25c depicts the self-healing of an Airy beam after propagating 10 cm in the same environment. Besides the anticipated drop in the beam intensity due to Mie scattering, the beam still exhibits in every respect its characteristic pattern.

1.4.6 Resilient Airy Beam Propagation in a Turbulent Medium

We have also studied the effect of turbulence on an Airy beam. The turbulent environment was realized over a heated rough accordion-shaped aluminum foil above which violent heat convection air currents were generated. The turbulence was controlled by adjusting the temperature of the hotplate around 300°F. The Airy beam was then passed right above the aluminum foil up to a distance of 8 cm. In all our experiments the resilience of the Airy beam (without any initial amplitude distortions) against turbulence was remarkable (see Fig. 1.26a and the related video file in [55]). To some extent this robustness can be qualitatively understood if one considers the phase structure of the beam: alternations in phase between 0's and π's result in zero-intensity regions and these singularities can be in turn extremely stable [56, 57]. For comparison purposes we turned off the cubic phase from the SLM, thus producing a comparable Gaussian beam. This diffracting Gaussian beam was then passed through the same turbulent system. Unlike the Airy beam, the Gaussian beam was strongly deformed and it suffered massive distortions (see Fig. 1.26b and the related video file in [58]).

Another experiment we did for self-healing of an Airy beam is to reposition the peak beam intensity to a target even through disordered media using the linear control method discussed in Sect. 1.3.3. This is illustrated in Fig. 1.27a, where the peak intensity of a truncated Airy beam is supposed to land on a target located at $(x, y, z) = (0, 0, 25\text{ cm})$ along a curved trajectory (red dashed curve) after

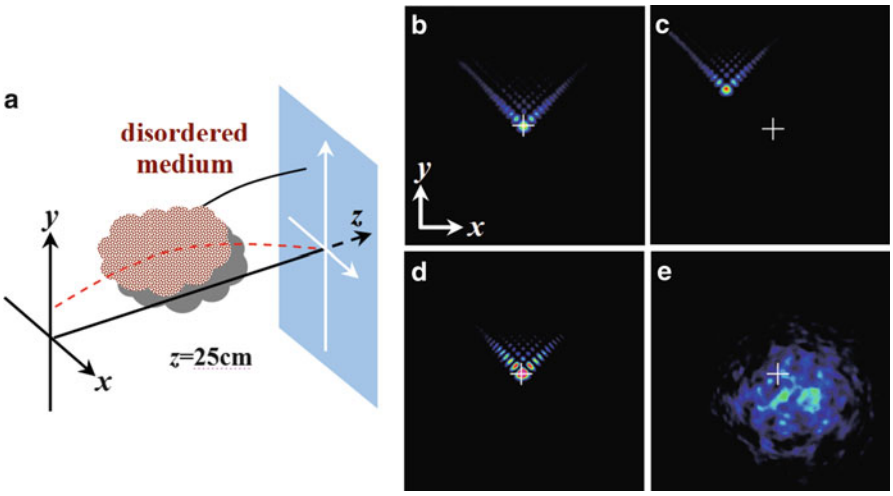

Fig. 1.27 (**a**) Schematic of Airy beam propagation through a disordered medium. The *red dashed* (*black solid*) *curve* depicts the trajectory in free-space (disordered medium); (**b**, **c**) intensity pattern of output Airy beam at $z = 25$ cm through air (**b**) and stirred salt–water mixture (**c**); (**d**) restoration of the Airy beam peak intensity at the target after translating the phase mask and input Gaussian beam; (**e**) typical output pattern of a Gaussian beam from the salt–water mixture. The *white cross* corresponds to the target point at (0, 0, 25 cm)

passing through a disordered medium. However, due to presence of the disordered media, the Airy beam path (black solid curve) is deflected off the target apart from diminishing intensity during propagation. Simply by translating the phase mask and the initial Gaussian beam, the restored peak intensity can be repositioned at the target. Corresponding experimental results obtained with a turbulent salt–water mixture are shown in Fig. 1.27b–e. First, we "aim" the Airy beam at the target after 25 cm of propagation through air. Then, salt is added and stirred in water placed in the beam path. Although the Airy beam is recovered through disordered scatters due to its self-healing property, its position in the target plane is shifted dramatically (Fig. 1.27c). The large lateral shift of the Airy beam path from Fig. 1.27b, c is caused mainly by refraction from the salt–water mixture (which has a refractive index different than that of air), while small variation of the Airy beam in its shape and location in a given output plane occurs due to turbulence of stirred mixture. By translating the mask and the Gaussian beam independently, as expected, not only the Airy beam comes back to the target, but also its peak intensity is restored (Fig. 1.27d). We emphasize that Fig. 1.27c, d were taken as a snapshot to show one example of the "fluctuating" pattern, as the shape and transverse position of the self-healing Airy beam vary slightly with time. However, the average intensity pattern is a well-defined Airy beam with its peak intensity repositioned at the target. For comparison, keeping all conditions unchanged as for Fig. 1.27d except for changing the cubic phase into uniform phase in the SLM, the Airy beam returns

to a normal Gaussian beam which is severely scattered, deformed and shifted after propagating through the same salt–water mixture (Fig. 1.27e). These results suggest that Airy beams are excellent candidates for beam reposition to a given target through disordered or turbulent media, perhaps even with a feed-back system that could compensate time-dependent fluctuation.

In detail, the evolution of Airy beam intensity distribution in turbulence was examined in [59], where results show that the centroid position and skewness of an Airy beam are independent of turbulence. In addition, the numerical work in [60] found that scintillation of an Airy beam array is significantly reduced in the turbulent atmosphere.

1.4.7 Restoration and Degeneration of Deformed Airy Beams

Previous sections investigated reconstruction of either perfect or imperfect (with missing lobes) Airy beams. In this section, we discuss the self-healing of deformed Airy beams, in which none of the Airy lobes are blocked but the angle between the two "wings" differs from the regular 90° for the perfect 2D Airy beams. The wave function of a deformed Airy beam studied here can be expressed by

$$U = \mathrm{Ai}(X/x_0)\exp(\alpha X/x_0)\mathrm{Ai}(Y/x_0)\exp(\alpha Y/x_0) \tag{1.42}$$

where X and Y are respectively equivalent to $(-\sqrt{r}x - y/\sqrt{r})/\sqrt{2}$ and $(\sqrt{r}x - y/\sqrt{r})/\sqrt{2}$, x_0 is a constant governing the size of the Airy beam, and r is the parameter determining the degree of deformation of the Airy beam. $r = 1$ corresponds to the normal case for which the angle between the two "wings" of the Airy beam is equal to 90° (Fig. 1.28a). After 20 cm of linear propagation, this regular Airy beam remains nearly diffraction free. For $r < 1$, the angle between the two wings of a deformed Airy beam is obtuse as depicted in Fig. 1.28b, c. In this case, the wings shrink gradually towards the 90° position during propagation, with a slight increase of its transverse acceleration (see Fig. 1.28b, c, bottom). Inversely, for $r > 1$, the angle between the two wings of a deformed Airy beam is acute as depicted in Fig. 1.28d, e, so the wings expand gradually towards the 90° position with a slight decrease of its acceleration. Interestingly, when the angle deviation from 90° is not too big, the deformed Airy beam seems to restore well during propagation, but at large deviations, the angle can change from obtuse to acute and vice verse. In particular, it is found that a strongly deformed 2D Airy beam with a small acute angle degenerates into a quasi-1D Airy beam, as can be seen from Fig. 1.28e. This was confirmed by more detailed simulations.

To perform experimental demonstration, a cubic phase mask is utilized as before (see inset in Fig. 1.29a). After 20 cm of propagation in free space, the Airy beam shifts vertically due to its transverse acceleration. Now we modify the vertical–horizontal length *ratio* of the phase mask, which controls the angle between the two wings.

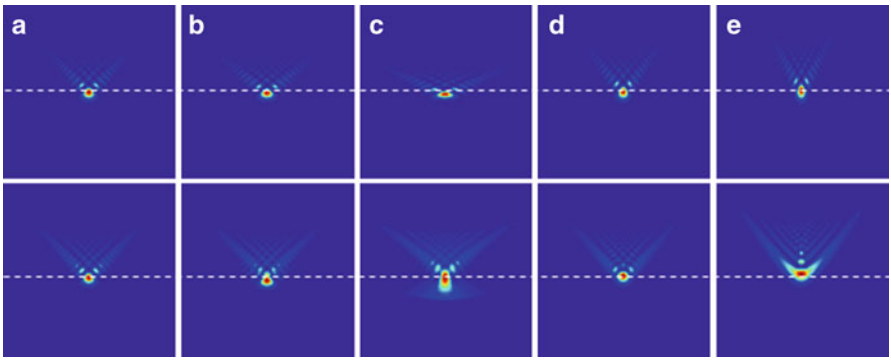

Fig. 1.28 Numerical simulations of linear propagation of deformed Airy beams. *Top* and *bottom panels* correspond to input and output after 20-cm propagation, respectively. From left to right, $r = 1, 0.89, 0.67, 1.11$, and 1.33. (**a**) A regular Airy beam at a right angle between the two wings, (**b**, **c**) deformed Airy beams at an obtuse angle, and (**d**, **e**) deformed Airy beams at an acute angle. *Dashed lines* mark the position of peak intensity of the regular Airy beam

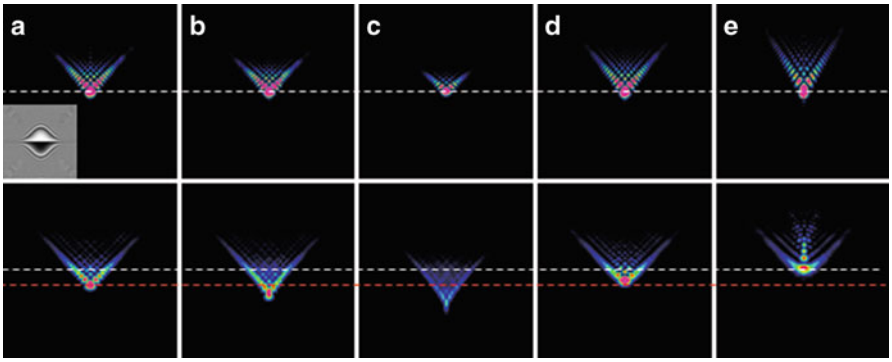

Fig. 1.29 Experimental observation of linear propagation of deformed Airy beams corresponding to Fig. 1.28. *Top* and *bottom panels* correspond to input and output after 20 cm propagation, respectively. The values of the parameter r are the same as in Fig. 1.28. The inset in (**a**) shows the unstretched cubic phase mask. The *white dashed lines* mark the position of peak intensity of the Airy beam at $z = 0$ cm, and the *red line marks* the position of peak intensity of the regular Airy beam at $z = 20$ cm (b, c) deformed Airy beams at an obtuse angle, and (d, e) deformed Airy beams at an acute angle.

We observe that the Airy beam indeed gradually opens its wings (Fig. 1.29b, c, top) when the ratio of the mask is reduced (i.e., the mask is stretched horizontally). After 20 cm propagation, the wings contract towards 90° position (Fig. 1.29b, c, bottom), in agreement with simulation. If the ratio is too small, the nondiffraction property of the Airy beam cannot persist, and the Airy beam cannot be restored as seen in Fig. 1.29c. Likewise, when the ratio of the mask is increased (i.e., the mask is stretched vertically), the wings expand and the angle of the Airy beam increases from an acute angle towards the 90° position (Fig. 1.29d, e). Apart from the wing flipping, another two

interesting observations merit mentioning: firstly, as compared to the perfect Airy beam, increased acceleration is observed for "expanded" Airy beam (Fig. 1.29b, c), whereas decreased acceleration for "compressed" Airy beam (Fig. 1.29d, e). The larger change in experiment as opposed to that in simulation is due to that the area of the phase mask (hence, the size of the deformed Airy beam) is not kept constant as the mask is stretched; secondly, when the Airy beam is strongly deformed at a very small acute angle, the 2D Airy beam cannot maintain, but rather degenerates into a quasi-1D Airy beam as seen from the bottom panel of Fig. 1.29e. The experimental results agree well with our numerical simulations.

In addition, Airy beams without standard shapes are also investigated in other aspects, such as, combining Airy beams with vortex [61, 62], reducing side lobs of Airy beams [63], etc. Self-healing dominates the propagation dynamics although some other interesting phenomena associated with these nonconventional Airy beams were discussed.

In summary, we have demonstrated both theoretically and experimentally the self-healing properties of optical Airy beams. By monitoring their internal transverse power flow we have provided insight concerning the self-healing mechanism of Airy beams. We have also experimentally shown that these optical beams can be robust in adverse environments such as in scattering and turbulent media. Furthermore, we have demonstrated that an Airy beam can retain its shape and structure under turbulent conditions as opposed to a comparable Gaussian beam that suffers from massive distortion. The robust nature of Airy beams may have important implications in other areas such as atmospheric propagation and microparticle manipulation as we shall discuss in Sect. 1.6.

1.5 Nonlinear Control and Generation of Airy Beams

1.5.1 Persistence and Breakdown of Airy Beams Driven by an Initial Nonlinearity

In this section, we study the transition of Airy beams from a nonlinear to a linear medium driven initially by a self-focusing or -defocusing nonlinearity. Some unique behaviors of such nonlinearity-controlled Airy beams, including loss or persistence of acceleration, normal or anomalous diffraction were observed. In particular, an Airy beam under an initial self-defocusing nonlinearity exhibits anomalous diffraction and propagates robustly over long distance after exiting the nonlinear medium, but it breaks down in both Airy-beam pattern and acceleration when driven by a self-focusing nonlinearity [64].

The experiments were performed in a biased 1 cm-long photorefractive SBN:60 crystal (Fig. 1.30a). As before, to create a truncated Airy beam, a SLM is placed at the focal plane of the Fourier transform lens. The Airy beam ($\lambda = 532$ nm) is extraordinarily polarized, propagating first through the biased crystal under the influence of photorefractive screening nonlinearity, and then through air (free-space) for

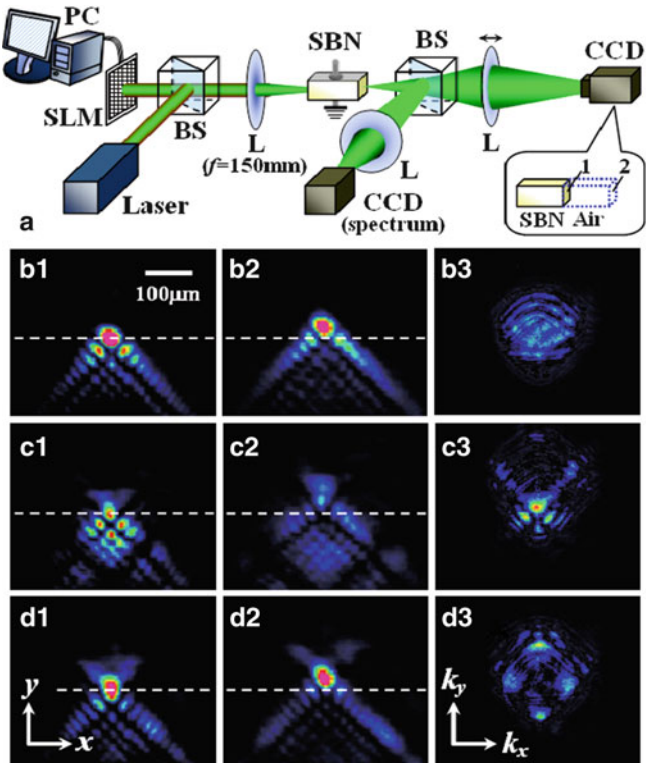

Fig. 1.30 (**a**) Schematic of experimental setup. *SLM* spatial light modulator, *SBN* strontium–barium niobate crystal. (**b–d**) Output intensity patterns of an Airy beam after 1 cm through crystal (1st column) plus another 1 cm through air (2nd column) when (**b**) no nonlinearity, (**c**) self-focusing and (**d**) self-defocusing nonlinearity is present. *White dashed line* marks the "head" position of the Airy beam at crystal output. The 3rd column shows Fourier spectra of the Airy beam corresponding to the 1st column)

another 1 cm. Solely by switching the polarity of the bias field, self-focusing and self-defocusing nonlinearity is achieved for nonlinear control of the Airy beam. The Airy beam patterns along with ***k***-space spectra are monitored by CCD cameras.

Typical experimental results are shown in Fig. 1.30b–d. When no bias field is present, the Airy beam undergoes linear propagation inside the crystal. (The photorefractive diffusion effect [65] can be neglected due to the large size of the Airy beam used here—about 50 μm for the main lobe). After another 1 cm of propagation in air, its main spot (or "head") is shifted along the vertical direction (Fig. 1.30b2) in comparison with that right at the existing face of the crystal (Fig. 1.30b1) due to the transverse acceleration. When a positive dc field of 4×10^4 V/m is applied, the Airy beam experiences a self-focusing nonlinearity and reduces its overall size with most of its energy distributed to the four spots close to the Airy head (Fig. 1.30c1). In this case, the nonlinearity seems to cause stagnation

of Airy beam's acceleration, and the subsequent free-space propagation shows that the Airy beam is strongly deformed by the nonlinearity (Fig. 1.30c2). In addition, its ***k***-space spectrum is "focused" towards the center (Fig. 1.30c3) as compared to the case without initial nonlinearity (Fig. 1.30b3), suggesting that the Airy beam exhibits normal diffraction. By reversing the polarity of the bias field (to -4×10^4 V/m) so that the Airy beam experiences a self-defocusing nonlinearity, its nonlinear output (Fig. 1.30d1) and subsequent linear propagation (Fig. 1.30d2) behave dramatically differently. The intensity profile of the Airy beam is less affected by the self-defocusing nonlinearity, and the peak intensity of the Airy beam after subsequent linear propagation in air is not decreased but rather increased while persistent in its acceleration. Furthermore, the Fourier spectrum reshapes into four major spots in ***k***-space as shown in Fig. 1.30d3, resembling the Broullion zone (BZ) spectrum and associated anomalous diffraction behavior in photonic lattices [66–68].

These experimental observations were corroborated with numerical simulations. Propagation of an Airy beam in a biased photorefractive crystal can be described by the following nonlinear Schrödinger equation

$$\frac{\partial U}{\partial z} = \frac{i}{2k_0 n_0}\left(\frac{\partial^2 U}{\partial x^2} + \frac{\partial^2 U}{\partial y^2}\right) + ik_0 \Delta n U, \tag{1.43}$$

where U is the wave function, k_0 is the vacuum wave vector, and $n_0 = 2.3$ is the unperturbed refractive index. In the biased crystal, the nonlinearity for an e-polarized beam can be determined by $\Delta n = -0.5 {n_0}^3 \gamma_{33} E_0/(1 + |U|^2)$, in which $\gamma_{33} = 280$ pm/V and E_0 is the amplitude of the bias field. The wave function of an input Airy beam can be expressed as $U(x, y, z = 0) = U_0 \mathrm{Ai}(X/x_0) \exp(\alpha X/x_0)$ $\mathrm{Ai}(Y/y_0) \exp(\alpha Y/y_0)$, where U_0 is the amplitude, Ai denotes the Airy function, X and Y are respectively equivalent to $(x + y)/\sqrt{2}$ and $(-x + y)/\sqrt{2}$, x_0 and y_0 are constants governing the transverse size of the Airy beam, and again α is the decay factor for the truncated beam profile.

Numerical simulations were performed by solving (1.43) with the split-step beam propagation method (parameters U_0, x_0, and α are chosen as 7.3, 13.5×10^{-6}, and 0.11, respectively). Numerical results corresponding to Fig. 1.30(c1–c3) under the self-focusing initial nonlinearity ($E_0 = +40$ kV/m) are shown in Fig. 1.31a–c. The propagation can be better visualized from the side-view evolution as shown in Fig. 1.31d, where the dashed curve marks the path of the same Airy beam without initial nonlinearity. Clearly, the acceleration is reduced or lost as compared to the case without the nonlinear control. In Fig. 1.31e–f, we plotted the transverse energy flow of the output beam corresponding to the areas marked in Fig. 1.31a, b. Apparently, after initial nonlinear propagation, the direction of the energy flow goes towards all directions, suggesting that the phase (and thus the acceleration) of the Airy beam is destroyed by the self-focusing nonlinearity. This might be due to that nonlinear trapping and interaction among waveguides induced by the lobes of the Airy beam destructed its phase relation.

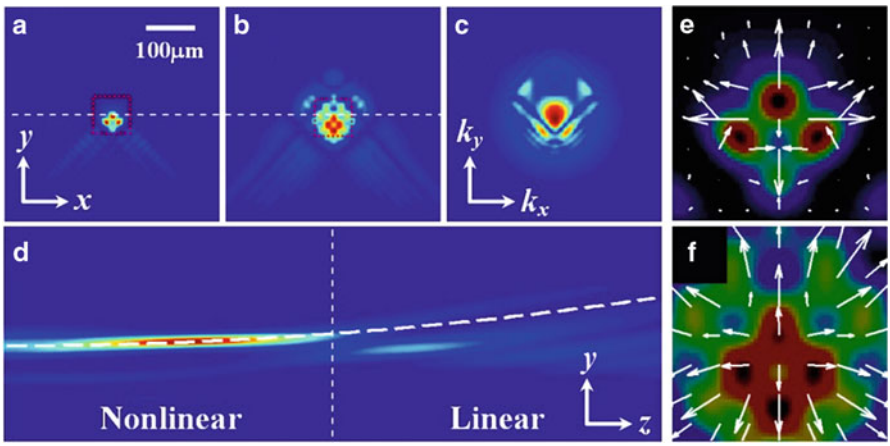

Fig. 1.31 Numerical simulation of an Airy beam propagating under an initial self-focusing nonlinearity. (**a**, **b**) Transverse intensity patterns after (**a**) 1 cm through crystal plus (**b**) another 1 cm through air. (**c**) Fourier spectrum of the output Airy beam. (**d**) Side-view of 2 cm-propagation, where the *dashed curve* represents the trajectory of the Airy beam without initial nonlinearity. (**e**, **f**) Calculated transverse energy flow around the main lobe corresponding to the *square area* shown in (**a**, **b**), respectively

Once the Airy beam is released into free-space, it behaves more like a confined Gaussian beam, showing normal diffraction without evident acceleration.

With a reversed bias field of $E_0 = -40$ kV/m, i.e., under the self-defocusing nonlinearity, our numerical results show that the Airy beam is somewhat expanded at the beginning due to the self-defocusing nonlinearity but its shape is nearly unchanged (Fig. 1.32a). In contrast to the self-focusing case, the Airy beam persists in its intensity pattern and transverse acceleration during subsequent free-space propagation (Fig. 1.32b, d). Furthermore, its power spectrum reshapes into a diamond-like pattern and is concentrated unevenly on four spots (Fig. 1.32c), resembling the first BZ [66] of an asymmetric square lattice. The energy-flow of the Airy beam is also quite different from that in the self-focusing case, since the Poynting vectors of the Airy beam line up towards the same direction around the Airy "head" (Figs. 1.32e, f). Counterintuitively, the peak intensity of the main lobe gets even stronger after subsequent linear propagation, as seen from the side-view evolution (Fig. 1.32d). This phenomenon suggests that the Airy beam might experience anomalous diffraction after initial self-defocusing nonlinearity, akin to that observed in photonic lattices [67, 68].

Indeed, if we zoom in the Airy-beam intensity pattern not far from the "head", it exhibits a square-like structure with nonuniform intensity distribution and lattice spacing. Under a self-defocusing nonlinearity, the Airy beam induces an index distribution akin to a nonuniform or chirped "backbone" lattice. This self-induced chirped lattice could exhibit properties similar to uniformed photonic lattices [69], thereby change the diffraction of the Airy beam. Using the BZ spectroscopy method [70, 71], we calculated the BZ spectrum of the induced lattice and found that the lattice

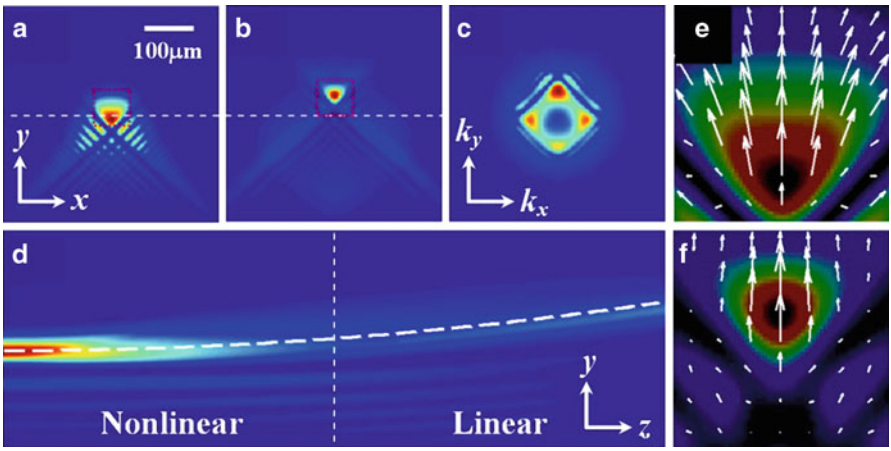

Fig. 1.32 Numerical simulation of an Airy beam propagating under an initial self-defocusing nonlinearity. Other description is the same as that for Fig. 1.31

self-induced by the Airy beam indeed shows a BZ structure [64]. Thus, the principle for anomalous diffraction observed here could be similar to that reported in [66, 68].

1.5.2 Nonlinear Generation and Control of Airy Beams

Airy beams are usually generated by using linear diffractive elements. Recently, Arie's group has proposed and demonstrated a method for nonlinear generation (i.e., through a nonlinear process) of Airy beams [29]. Specifically, it was done by a second harmonic generation (SHG) process through the design and fabrication of an asymmetric quadratic nonlinear photonic structure. The asymmetric structure induces a cubic phase front to the generated SHG output, whose Fourier transform is an accelerating Airy beam. This nonlinear generation process enables Airy beams to be obtained at new wavelengths. Indeed, frequency doubling of 1D and 2D Airy beams in a periodically poled crystal has been achieved in their experiment [72].

In addition, it was suggested theoretically that the generation of Airy beams by nonlinear processes opens several possibilities for controlling and manipulating these beams. As an example, the same group experimentally demonstrated a method to control the relative intensity along the caustic of nonlinearly generated Airy beams by controlling the phase matching conditions of the nonlinear interaction via temperature tuning. By analyzing the interactions in the Fourier space, they showed that the shaping of the beams is achieved by having noncollinear interactions. Furthermore, they studied the possibilities for

all optical control by changing the pump wavelength. This includes for example nonlinear control of the beam acceleration direction, the wavelength of the output Airy beam, and the location of the Airy beam peak intensity along the same curved trajectory [73, 74].

1.5.3 Nonlinear Self-trapping of Airy-like Optical Beams

As discussed above, in practice, all nondiffracting Airy beams must be truncated, to keep the energy finite. Such truncated beams eventually diffract and lose their unique structure after long enough linear propagation. Thus, recently, research efforts have also been devoted to identify nonlinear physical mechanisms that could allow these highly localized wave packets to propagate in a true diffraction-free manner, as in the case of optical spatial solitons [75, 76].

It is well known that self-focusing can counteract the effects of dispersion and diffraction, leading to formation of optical solitons. Spatial soliton beams are usually symmetric, due to the even (second-order) nature of diffraction, and the typical nonlinear responses are local and conservative. However, more complex responses, such as the gradient-sensitive diffusion nonlinearity, can lead to a whole different class of instability and dynamics. In particular, it was suggested that highly asymmetric nonlinear action such as diffusion nonlinearity experienced by an asymmetric beam could lead to invariant propagation of the beam. The prospect of observing a diffusion-trapped exponentially contained Airy wave packet in nonlinear photorefractive media with diffusion nonlinearity was first proposed in [24]. Recently, Fleischer's group has reported the experimental observation of self-trapped Airy beams in a nonlinear medium. As opposed to screening or photovoltaic spatial solitons [75] this new class of self-localized beams owes its existence to carrier diffusion effects. The asymmetric action of two-wave mixing supports the asymmetric intensity profile of the Airy states, with a balance that is independent of the beam intensity. Furthermore, the self-trapped wave packets self-bend during propagation at an acceleration rate that is independent of the thermal energy associated with the diffusive nonlinearity. These results represent the first example of Airy solitary-like wave formation using two-wave mixing [77].

Quite recently, Segev's group has studied self-accelerating self-trapped beams in nonlinear optical media, exhibiting self-focusing and self-defocusing Kerr and saturable nonlinearities, as well as a quadratic response. In Kerr and saturable media such beams are stable under self-defocusing and weak self-focusing, whereas for strong self-focusing the beams off-shoot solitons while their main lobe continues to accelerate. These self-trapped Airy-like accelerating beams in nonlinear media propagate along parabolic trajectories and their existence curve of nonlinear generation was derived [78].

1.6 Proposed Applications

1.6.1 Optically Clearing Particles Using Airy Beams

Nondiffracting beams, such as the Bessel beam, Mathieu beam, and Airy beam, do not spread as they propagate. This property is particular useful in many applications include imaging, micromanipulation, and optical transfection.

Perhaps, one of the exciting applications of Airy beams is particle transportation and clearing along the curved paths as proposed by Dholakia's group [14]. They employed micrometer-sized colloidal particles, although their experiment can be extended directly to other chemical samples or even biological matter. As seen from Fig. 1.9a, a 2D truncated Airy beam has the form of a main spot and a number of side lobes whose intensity decays with increasing distance from the main spot, which induces optical gradient forces dragging dielectric particles towards the main spot. Then, these particles are guided along a projective trajectory as the Airy beams propagate and accelerate transversely. In their experimental setup, a finite Airy beam is used as a form of micrometer-sized "snowblower" at the bottom to blow the particles upwards and sideways. Without any motion of the light field, these samples are cleared towards the direction where the trajectory of the Airy beams point to. Due to the self-healing property of the Airy beams, such optically mediated particle clearing could be made more robust. The advanced "optical path clearing (OPC)" method mediated with Airy beams was demonstrated in the following work of Dholakia's group [79]. Rotating multiple Airy beams were used for clearing regions in a sample in a synchronized effort. The authors also suggested that the improvement for both clearing performance and efficiency might be achieved by utilizing dynamic multiple-step clearing approaches based on multiple Airy beams operated according to a time-sharing protocol.

1.6.2 Generation of Curved Plasma Channels by Airy Beams

In early studies, the plasma channels generated by femtosecond laser pulse were always along straight lines. Thus, conical radiation originating from straight filaments at different longitudinal sections of the beam overlaps in the observation plane, making the analysis of the emission more complicated. To solve this problem, femtosecond laser beams with a transverse spatial pattern in the form of a 2D Airy function were employed to write curved plasma channels by Moloney's group in collaboration with Christodoulides' group. Broadband emission from different longitudinal sections of the filament is therefore along angularly separated paths, resulting in the spatial separation of this emission in the far field. This technology has been successfully applied to different media: air and water, for which, the self-focusing collapse of the beam to a singularity is respectively arrested by plasma defocusing and the group-velocity dispersion [17, 18].

1.6.3 Generation and Control of Plasmonic Airy Beams

Another exciting application of Airy beams is their possible use in routing plasmonic energy. One-dimensional Airy beams have recently been introduced theoretically by Christodoulides' group into the field of plasmonics as the only nondiffracting solution in the planar systems of metal interfaces [21]. The analysis indicates that a new class of surface plasmons could be introduced that can freely self-bend during propagation. Due to the strong confinement of surface plasmon polaritons, the plasmonic Airy beams could be a promising candidate for subwavelength beam manipulation and on-chip signal processing in the emerging field of nanoplasmonics. Recently, Kivshar's group has proposed theoretically plasmonic Airy beam manipulation by means of linear potentials created by a wedged metal–dielectric–metal structure with one titling metal plate. They showed that the plasmonic Airy beam deflection could be enhanced, compensated, or even reversed, while still maintaining the self-healing properties [80].

Quite recently, the race for experimental generation and control of plasmonic Airy beams has accelerated, and there are at least three independent groups that reported successful demonstration of Airy surface plasmons [81–83]. In these studies, the observed Airy plasmons were excited on a metal–air interface using specially designed diffraction grating by taking advantage of the subwavelength confinement and localized propagation of tightly localized surface plasmon polaritons. The propagation of Airy Plasmon along curved parabolic trajectories was directly observed, together with their self-healing phenomenon after passing through surface defects. In particular, it was shown that the ballistic motion of the Airy plasmons could be reconfigured in real-time by either a computer addressed spatial light modulator or mechanical means [81].

1.6.4 Optical Manipulation with Morphing Autofocusing Airy Beams

Beam focusing has always been a subject of practical importance. For many applications it is desirable to have a wavefront's energy abruptly autofocused right onto a target while maintaining a low intensity profile up until that point. This feature could be useful, for example, in biomedical treatments and other nonlinear settings such as optical filamentation. Lately, a new class of autofocusing waves, as mentioned in Sect. 1.2.5, based on Airy beams has been proposed [38, 39] and observed [41, 42]. These field configurations rely on radially symmetric or circular Airy beams, and they can be established entirely on linear effects, i.e., without invoking any nonlinear self-focusing processes. In addition, a recent theoretical study has also indicated that a superposition of Airy wavelets can asymptotically "morph" into Bessel beams in their far-field [84].

Of particular interest is the potential application of these abruptly autofocusing beams. One example is processing of a thick sample by laser ablation [41]. Another

example is optical guiding of nonabsorbing microparticles [15]. In the latter example demonstrated by Chen's group, an abruptly autofocusing beam was sent into an optical tweezers-like setting, where the particles were trapped and transported along the autofocusing beam. It was suggested that the circular autofocusing Airy beam might be used as a tapered channel guide for microparticles [15].

1.7 Summary

In this chapter, we provide an overview on self-accelerating Airy beams, their generation, control, and potential applications. As mentioned, driven by both fundamental interest and application potential, the number of research papers dealing with optical Airy beams soared in the last a few years, accompanied with new discoveries and surprising results. We envision that the research on self-accelerating Airy beams will keep its accelerating momentum in years to come.

This work was supported by the US National Science Foundation, the Air Force Office of Scientific Research, and by the 973 program, the National Natural Science Foundation of China (NSFC), and the Program for Changjiang Scholars and Innovative Research Team in China.

References

1. M.V. Berry, N.L. Balazs, Am. J. Phys. **47**, 264 (1979)
2. K. Unnikrishnan, A.R.P. Rau, Am. J. Phys. **64**, 1034 (1996)
3. J. Durnin, J. Opt. Soc. Am. A **4**, 651 (1987)
4. J. Durnin, J.J. Miceli, J.H. Eberly, Phys. Rev. Lett. **58**, 1499 (1987)
5. J.C. Gutiérrez-Vega, M.D. Iturbe-Castillo, S. Chávez-Cerda, Opt. Lett. **25**, 1493 (2000)
6. M.A. Bandres, J.C. Gutiérrez-Vega, S. Chávez-Cerda, Opt. Lett. **29**, 44 (2004)
7. D. McGloin, K. Dholakia, Contemp. Phys. **46**, 15 (2005)
8. R. Stützle et al., Phys. Rev. Lett. **95**, 110405 (2005)
9. L.I. Schiff, *Quantum Mechanics*, 3rd edn. (McGraw-Hill, New York, NY, 1968)
10. F. Gori, G. Guattari, C. Podovani, Opt. Commun. **64**, 491 (1987)
11. J. Durnin, J.J. Miceli, J.H. Eberly, Phys. Rev. Lett. **66**, 838 (1991)
12. G.A. Siviloglou, D.N. Christodoulides, Opt. Lett. **32**, 979 (2007)
13. G.A. Siviloglou, J. Broky, A. Dogariu, D.N. Christodoulides, Phys. Rev. Lett. **99**, 213901 (2007)
14. J. Baumgartl, M. Mazilu, K. Dholakia, Nat. Photonics **2**, 675 (2008)
15. P. Zhang, J. Prakash, Z. Zhang, M.S. Mills, N.K. Efremidis, D.N. Christodoulides, Z. Chen, Opt. Lett. **36**, 2883 (2011)
16. Z. Zheng, B. Zhang, H. Chen, J. Ding, H. Wang, Appl. Opt. **50**, 43 (2011)
17. P. Polynkin, M. Kolesik, J.V. Moloney, G.A. Siviloglou, D.N. Christodoulides, Science **324**, 229 (2009)
18. P. Polynkin, M. Kolesik, J. Moloney, Phys. Rev. Lett. **103**, 123902 (2009)
19. J. Li, W. Zang, J. Tian, Opt. Exp. **18**, 7300 (2010)
20. J. Li, X. Fan, W. Zang, J. Tian, Opt. Lett. **36**, 648 (2011)
21. A. Salandrino, D.N. Christodoulides, Opt. Lett. **35**, 2082 (2010)
22. D.M. Greenberger, Am. J. Phys. **48**, 256 (1980)

23. O. Vallée, M. Soares, *Airy Functions and Applications to Physics* (Imperial College Press, London, 2004)
24. D.N. Christodoulides, T.H. Coskun, Opt. Lett. **21**, 1460 (1996)
25. I.M. Besieris, A.M. Shaarawi, Opt. Lett. **32**, 2447 (2007)
26. I.M. Besieris, A.M. Shaarawi, R.W. Ziolkowski, Am. J. Phys. **62**, 519 (1994)
27. D.M. Cottrell, J.A. Davis, T.M. Hazard, Opt. Lett. **34**, 2634 (2009)
28. H.T. Dai, X.W. Sun, D. Luo, Y.J. Liu, Opt. Exp. **17**, 19365 (2009)
29. T. Ellenbogen, N. Voloch, A. Ganany-Padowicz, A. Arie, Nat. Photonics **3**, 395 (2009)
30. D.G. Papazoglou, S. Suntsov, D. Abdollahpour, S. Tzortzakis, Phys. Rev. A **81**, 061807(R) (2010)
31. S. Longhi, Opt. Lett. **36**, 716 (2011)
32. A. Efimov, C. Schaffer, D.H. Reitze, J. Opt. Soc. Am. B **12**, 1968 (1995)
33. M. Miyagi, S. Nishida, Appl. Opt. **18**, 678 (1979)
34. D.N. Christodoulides, N.K. Efremidis, P. Di Trapani, B.A. Malomed, Opt. Lett. **29**, 1446 (2004)
35. M. Weiner, Rev. Sci. Instrum. **71**, 1929 (2000)
36. D. Abdollahpour, S. Suntsov, D.G. Papazoglou, S. Tzortzakis, Phys. Rev. Lett. **105**, 253901 (2010)
37. A. Chong, W. Renninger, D.N. Christodoulides, F.W. Wise, Nat. Photonics **4**, 103 (2010)
38. N.K. Efremidis, D.N. Christodoulides, Opt. Lett. **35**, 4045 (2010)
39. I. Chremmos, N.K. Efremidis, D.N. Christodoulides, Opt. Lett. **36**, 1890 (2011)
40. E. Greenfield, M. Segev, W. Walasik, O. Raz, Phys. Rev. Lett. **106**, 213902 (2011)
41. D.G. Papazoglou, N.K. Efremidis, D.N. Christodoulides, S. Tzortzakis, Opt. Lett. **36**, 1842 (2011)
42. P. Zhang, J. Prakash, Z. Zhang, Y. Hu, N. K. Efremidis, V. Kajorndejnukul, D. N. Christodoulides, and Z. Chen, CLEO:QELS-Fundamental Science, paper QThS7 (2011)
43. J.W. Goodman, *Introduction to Fourier Optics*, 3rd edn. (Roberts & Company Publishers, Greenwood Village, CO, 2005)
44. G.A. Siviloglou, J. Broky, A. Dogariu, D.N. Christodoulides, Opt. Lett. **33**, 207 (2008)
45. Y. Hu, P. Zhang, C. Lou, S. Huang, J. Xu, Z. Chen, Opt. Lett. **35**, 2260 (2010)
46. Z. Ye, S. Liu, C. Lou, P. Zhang, Y. Hu, D. Song, J. Zhao, Z. Chen, Opt. Lett. **36**, 3230 (2011)
47. N.K. Efremidis, Opt. Lett. **36**, 3006 (2011)
48. V. Garces-Chavez, D. McGloin, H. Melville, W. Sibbett, K. Dholakia, Nature **419**, 145 (2002)
49. Z. Bouchal, J. Wagner, M. Chlup, Opt. Commun. **151**, 207 (1998)
50. L. Allen, M.W. Beijersbergen, R.J.C. Spreeuw, J.P. Woerdman, Phys. Rev. A **45**, 8185 (1992)
51. J. Broky, G.A. Siviloglou, A. Dogariu, D.N. Christodoulides, Opt. Exp. **16**, 12880 (2008)
52. C. Hwang, D. Choi, K. Kim, B. Lee, Opt. Exp. **18**, 23504 (2010)
53. H.C. van de Hulst, *Light Scattering by Small Particles* (Dover Publication Inc., New York, NY, 1981)
54. S. Prahl, http://omlc.ogi.edu/calc/mie_calc.html (2008)
55. http://www.opticsinfobase.org/abstract.cfm?URI=oe-16-17-12880 (Media 1)
56. J.F. Nye, M.V. Berry, Proc. R. Soc. London, Ser. A **336**, 165 (1974)
57. A. Dogariu, S. Amarande, Opt. Lett. **28**, 10 (2003)
58. http://www.opticsinfobase.org/abstract.cfm?URI=oe-16-17-12880 (Media 2)
59. X. Chu, Opt. Lett. **36**, 2701 (2011)
60. Y. Gu, G. Gbur, Opt. Lett. **35**, 3456 (2010)
61. H.T. Dai, Y.J. Liu, D. Luo, X.W. Sun, Opt. Lett. **35**, 4075 (2010)
62. H.T. Dai, Y.J. Liu, D. Luo, X.W. Sun, Opt. Lett. **36**, 1617 (2011)
63. S. Barwick, Opt. Lett. **36**, 2827 (2011)
64. Y. Hu, S. Huang, P. Zhang, C. Lou, J. Xu, Z. Chen, Opt. Lett. **35**, 3952 (2010)
65. S. Jia, J. Lee, G.A. Siviloglou, D.N. Christodoulides, J.W. Fleischer, Phys. Rev. Lett. **104**, 253904 (2010)
66. X. Wang, A. Bezryadina, Z. Chen, K.G. Makris, D.N. Christodoulides, G.I. Stegeman, Phys. Rev. Lett. **98**, 123903 (2007)
67. T. Pertsch, T. Zentgraf, U. Peschel, A. Bräuer, F. Lederer, Phys. Rev. Lett. **88**, 093901 (2002)
68. P. Zhang, C. Lou, S. Liu, J. Zhao, J. Xu, Z. Chen, Opt. Lett. **35**, 892 (2010)
69. M.I. Molina, Y.V. Kartashov, L. Torner, Y.S. Kivshar, Opt. Lett. **32**, 2668 (2007)

70. G. Bartal, O. Cohen, H. Buljan, J.W. Fleischer, O. Manela, M. Segev, Phys. Rev. Lett. **94**, 163902 (2005)
71. S. Liu, P. Zhang, X. Gan, F. Xiao, J. Zhao, Appl. Phys. B **99**, 727 (2010)
72. I. Dolev, A. Arie, Appl. Phys. Lett. **97**, 171102 (2010)
73. I. Dolev, T. Ellenbogen, A. Arie, Opt. Lett. **35**, 1581 (2010)
74. I. Dolev, T. Ellenbogen, N. Voloch-Bloch, A. Arie, Appl. Phys. Lett. **95**, 201112 (2009)
75. G.I. Stegeman, M. Segev, Science **286**, 1518 (1999)
76. D.N. Christodoulides, F. Lederer, Y. Silberberg, Nature **424**, 817 (2003)
77. S. Jia, J. Lee, J.W. Fleischer, G.A. Siviloglou, D.N. Christodoulides, Phys. Rev. Lett. **104**, 253904 (2010)
78. I. Kaminer, M. Segev, D.N. Christodoulides, Phys. Rev. Lett. **106**, 213903 (2011)
79. J. Baumgartl, T. Čižmár, M. Mazilu, V.C. Chan, A.E. Carruthers, B.A. Capron, W. McNeely, E.M. Wright, K. Dholakia, Opt. Exp. **18**, 17130 (2010)
80. W. Liu, D.N. Neshev, I.V. Shadrivov, A.E. Miroshnichenko, Y.S. Kivshar, Opt. Lett. **36**, 1164 (2011)
81. P. Zhang, S. Wang, Y. Liu, X. Yin, C. Lu, Z. Chen, X. Zhang, Opt. Lett. **36**, 3191 (2011)
82. A. Minovich, A.E. Klein, N. Janunts, T. Pertsch, D.N. Neshev, Y.S. Kivshar, Phys. Rev. Lett. **107**, 116802 (2011)
83. L. Li, T. Li, S.M. Wang, S.N. Zhu, Phys. Rev. Lett. **107**, 126804 (2011)
84. C. Hwang, K. Kim, B. Lee, Opt. Exp. **19**, 7356 (2011)